

## RESEARCH ARTICLE

10.1002/2015JB012548

## Key Points:

- New approach for extracting information on crustal structure from waveforms of microearthquakes
- Joint focal mechanism analysis, waveform stacking, and inversion result in topography of interfaces
- Application to KTB 2000 fluid injection microseismicity and swarm seismicity in West Bohemia

## Supporting Information:

- Letter S1

## Correspondence to:

P. Hrubcová,  
pavla@ig.cas.cz

## Citation:

Hrubcová, P., V. Vavryčuk, A. Boušková, and M. Bohnhoff (2016), Shallow crustal discontinuities inferred from waveforms of microearthquakes: Method and application to KTB Drill Site and West Bohemia Swarm Area, *J. Geophys. Res. Solid Earth*, 121, 881–902, doi:10.1002/2015JB012548.

Received 23 SEP 2015

Accepted 8 JAN 2016

Accepted article online 11 JAN 2016

Published online 18 FEB 2016

## Shallow crustal discontinuities inferred from waveforms of microearthquakes: Method and application to KTB Drill Site and West Bohemia Swarm Area

Pavla Hrubcová<sup>1</sup>, Václav Vavryčuk<sup>1</sup>, Alena Boušková<sup>1</sup>, and Marco Bohnhoff<sup>2,3</sup>
<sup>1</sup>Institute of Geophysics, Czech Academy of Sciences, Prague, Czech Republic, <sup>2</sup>Helmholtz Centre Potsdam GFZ, Potsdam, Germany, <sup>3</sup>Free University Berlin, Berlin, Germany

**Abstract** The waveforms of microearthquakes are of high frequency and complicated. They contain many phases secondarily generated at crustal interfaces and at small-scale inhomogeneities. They are highly sensitive to focal mechanisms and thus very different for each station of local networks. However, with a large number of microearthquakes, the scattered waves present in the waveforms can serve for identifying the prominent crustal discontinuities and for determining their depth. In this paper, we develop a new approach for extracting information on crustal structure from such waveforms and apply it for determining depth and lateral variations of crustal discontinuities. We show that strong dependence of microseismic waveforms on radiation pattern requires good station coverage and knowledge of focal mechanisms of the microearthquakes. Analysis of real observations is supported by waveform modeling and by analysis of radiation patterns of scattered waves. The robustness of the inversion for depth of crustal interfaces is achieved by stacking of a large number of waveforms and by applying a grid search algorithm. The method is demonstrated on two microseismic data sets of different origin: microseismicity induced during the Continental Super-Deep Drilling Project (KTB) 2000 fluid injection experiment and natural seismicity in the West Bohemia swarm region. High-frequency conversions at the KTB site indicate a prominent interface at depths of 2.3–4.1 km consistent with previous interpretations. Geologically, it may represent the contact of granitoids with much faster metabasites underneath. Seismicity in West Bohemia indicates a strong-contrast interface at depths of 3.5–6.0 km. This interface is in agreement with previous profiling and might be related to trapping of fluid emanations ascending from the mantle.

## 1. Introduction

In seismology, the crustal structure is usually studied by active seismic experiments with reflection and refraction seismic profiling or passive seismic experiments targeted on receiver function interpretations [e.g., Langston, 1979; Ammon *et al.*, 1990; Korenaga *et al.*, 2000; Hrubcová and Šroda, 2015]. The velocity models from both types of seismic studies are often inconsistent because of differences in ray coverage, frequency bands of studied waves, spatial resolution, and/or the uncertainties in the  $V_p/V_s$  ratio [Hrubcová and Geissler, 2009]. To overcome such discrepancies and to improve the velocity model, local microseismic data can serve as additional information for extracting the structure. Local earthquakes generate high-frequency seismic waves which can be reflected and converted at deep and/or shallow crustal interfaces and scattered at small-scale inhomogeneities [Aki, 1969]. Analyzing data which have been recorded at densely deployed local stations with a good azimuthal coverage at a target area, we can retrieve a detailed velocity model with an unprecedented accuracy.

The microseismic crustal studies have several advantages. First, they typically handle large amount of data ideal for stacking [Mayne, 1962; Yilmaz, 2001]. Second, microseismic sources are usually located at depths below the shallowest structure; hence, the waveforms are not so influenced by multiple scattering as data from explosions buried at the Earth's surface [Sato and Fehler, 1998]. Third, the data acquisition is not expensive. Fourth, a continuous monitoring of microseismicity provides a possibility to study temporal changes in velocity, associated, for example, with fluid flow or variations of tectonic stress [Rebâi *et al.*, 1992; Fisher and Becker, 2000; Koerner *et al.*, 2004; Copley and McKenzie, 2007]. All these facts underline the importance of microseismicity for studying detailed 3-D crustal structure.

A novel concept for extracting crustal structure from high-frequency waveforms of local earthquakes is applied to determine depth and topography of crustal discontinuities. The depth of discontinuities is modeled using

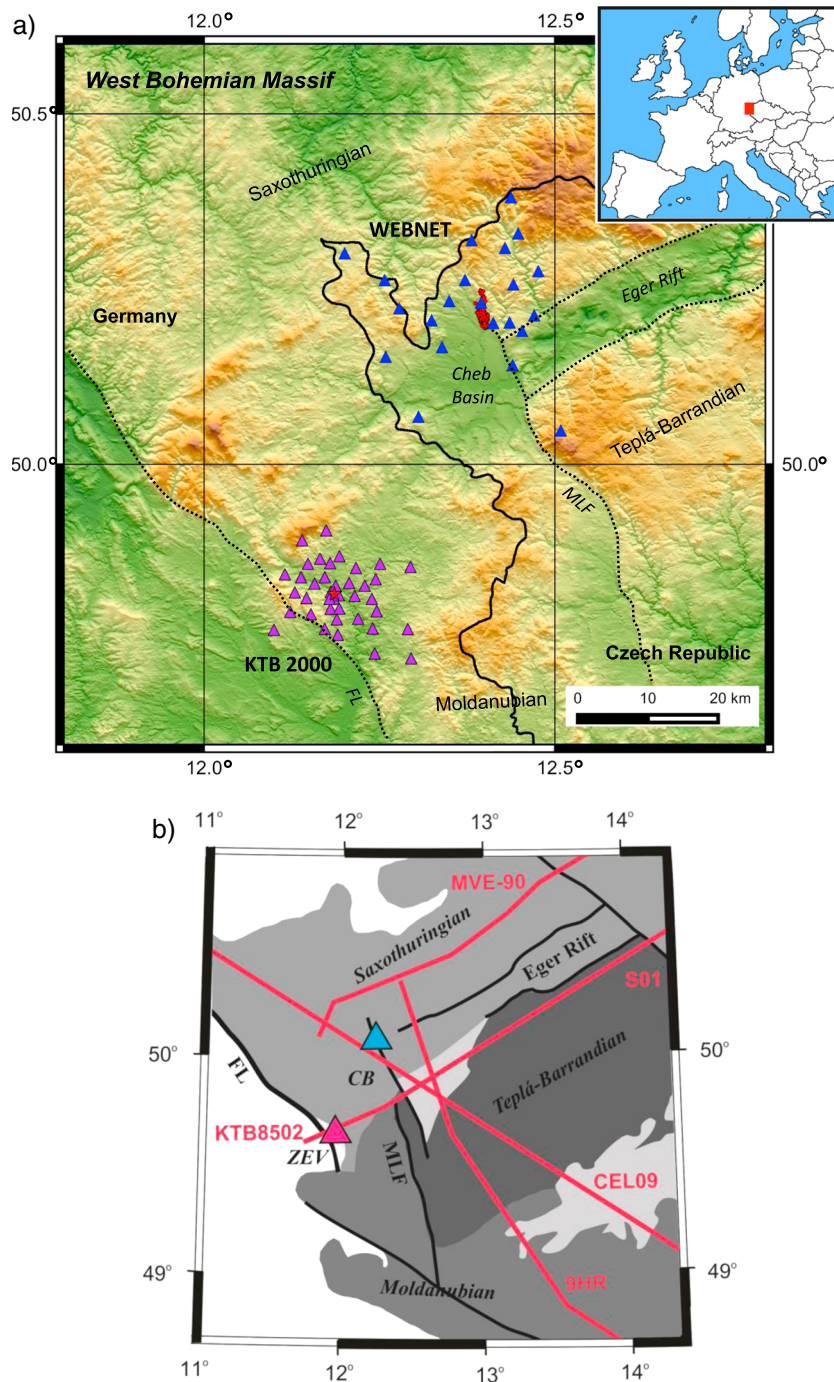


**Figure 1.** (a) Topography of the west part of the Bohemian Massif. Seismic stations of the KTB 2000 injection experiments are marked by violet triangles; epicenters of induced seismicity in the main hole marked by red star. WEBNET seismic stations are marked by blue triangles; epicenters of 2008 swarm marked by red dots. (b) Seismic reflection/refraction profiles (red lines) and superposition of the main tectonic units in West Bohemia. MLF, Mariánské Lázně Fault; FL, Franconian Lineament; CB, Cheb Basin; and ZEV, Zone of Erbendorf-Vohenstrauss.

several independent tools provided by refraction and reflections seismics combined with the earthquake source analysis. We use ray tracing [Červený, 2001] for calculating travel times of converted and/or reflected phases, analysis of focal mechanisms, and radiation patterns for converted/reflected phases, full waveform modeling using the discrete wave number method for comparing synthetic full wavefields with observed data,

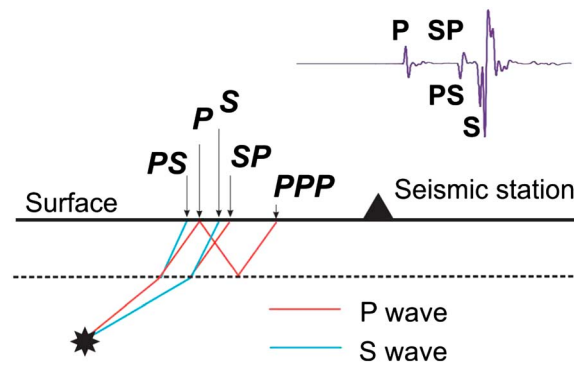


**Figure 2.** Schematic sketch showing the origin of the converted *SP* and *PS* phases and the reflected *PPP* phases at shallow crustal discontinuities.

alignment of traces and their stacking for amplifying studied phases, and a grid search method for the inversion.

The presented method is numerically tested on synthetic data. The applicability of the method is demonstrated on two microseismic data sets of different origin: (i) induced microseismic events of the Continental Super-Deep Drilling Project (KTB) 2000 fluid injection experiment and (ii) natural swarm seismicity in the West Bohemia region. Apart from different origin, both data sets come from regions with similar tectonic evolution, since they are situated at the western margin of the Bohemian Massif, a large Variscan complex terrain in central Europe (Figure 1).

## 2. Method of Detection of Shallow Discontinuities From High-Frequency Waveforms of Microearthquakes

### 2.1. Microseismic Data

Microseismic data represent seismic waves generated by weak local earthquakes. The number of microearthquakes is usually large and their hypocenters are clustered in space and time. The waveforms are of high frequency and very responsive to local crustal heterogeneities. The waveforms typically display distinct direct *P* and *S* waves followed by coda waves. The reflected *PPP* and converted *SP* and *PS* waves secondarily generated at subsurface layers represent the most pronounced coda phases (Figure 2). These phases can serve for detecting discontinuities within the crust and for determining their depth. If the microseismicity is monitored by a dense network of sensitive seismic stations with a good azimuthal distribution, it is possible to retrieve a detailed crustal structure and to map lateral variations and topography of crustal discontinuities.

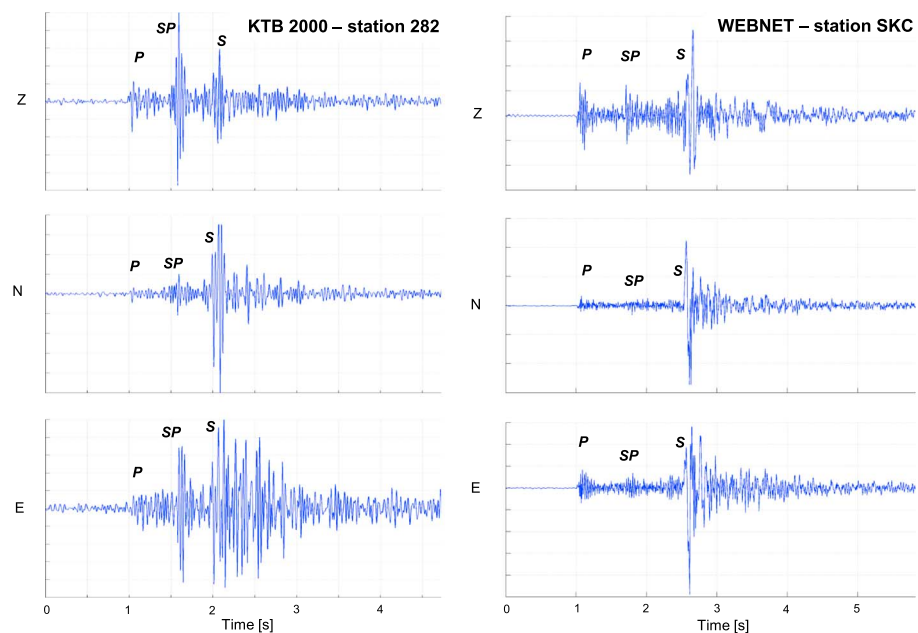


**Figure 3.** Example of three-component high-frequency velocity waveforms recorded at (left column) station 282 of the KTB 2000 network (event 023204, filtered by 10–40 Hz, depth 5.6 km, and local magnitude 0.82) and (right column) station SKC of the WEBNET network (event X3372A, filtered by 2.5–30 Hz, depth 10.1 km, and local magnitude 1.5). Note the *SP* conversions in both 3C data.

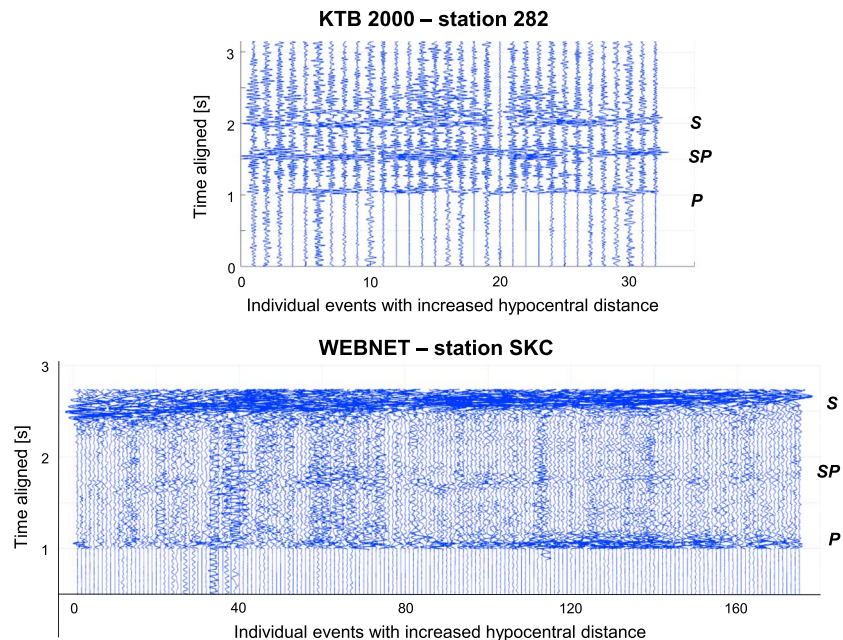


**Figure 4.** Example of the vertical component high-frequency velocity waveforms recorded at station 282 of the KTB 2000 network (filtered by 10–40 Hz and hypocentral distance 7.1–7.7 km) and station SKC of the WEBNET network (filtered by 2.5–30 Hz and hypocentral distance 11.2–13.1 km). Data presented in multitrace/seismic section view (each trace represents an individual event recorded at one common station plotted according to the increasing hypocentral distance) with the *P* wave alignment at 1 s. Note the converted *SP* phases generated at a shallow subsurface structure.

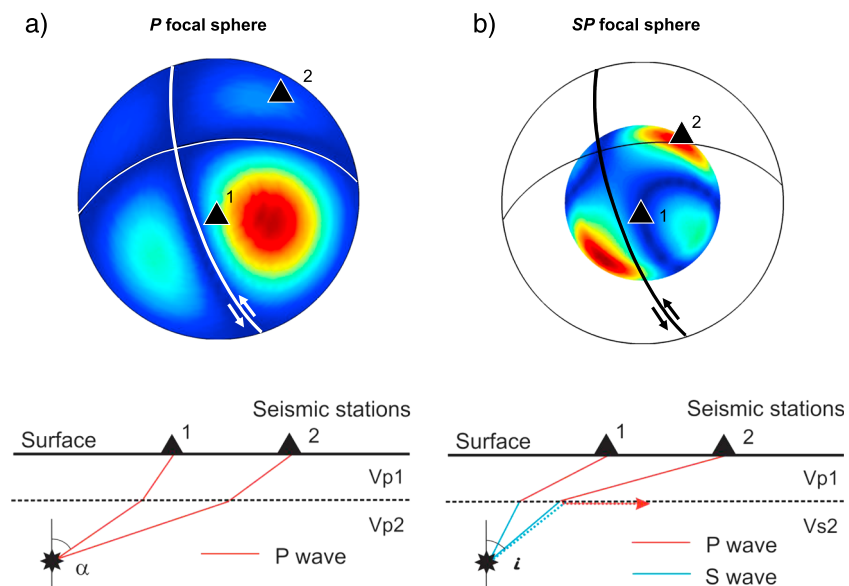


**Figure 5.** Prevailing focal mechanism dominant in the 2008 West Bohemian swarm with marked fault plane and projections of two seismic stations. (a) Amplitude of direct *P* waves projected on the *P* focal sphere. (b) Amplitude of converted *SP* waves projected on the *SP* focal sphere. Focal spheres are amplitude normalized from blue (minimum) to red (maximum). (bottom row) Schematic sketches showing the rays for the direct *P* wave and for the converted *SP* wave. Angle  $\alpha$  is the takeoff angle (i.e., the deviation of a ray from the vertical axis); angle  $i$  is the takeoff angle for the critical *SP* wave; and for  $\alpha > i$ , no *SP* rays (marked by dashed line) can be detected at the surface (due to  $V_{p1} > V_{s2}$ ). 1 = near station and 2 = distant station. Note the changes in the position of respective stations on the *P* and *SP* focal spheres. The *P* focal sphere is not symmetric with respect to the nodal lines because the corresponding moment tensor is not pure double couple but partly consists of negative isotropic and compensated linear vector dipole components.



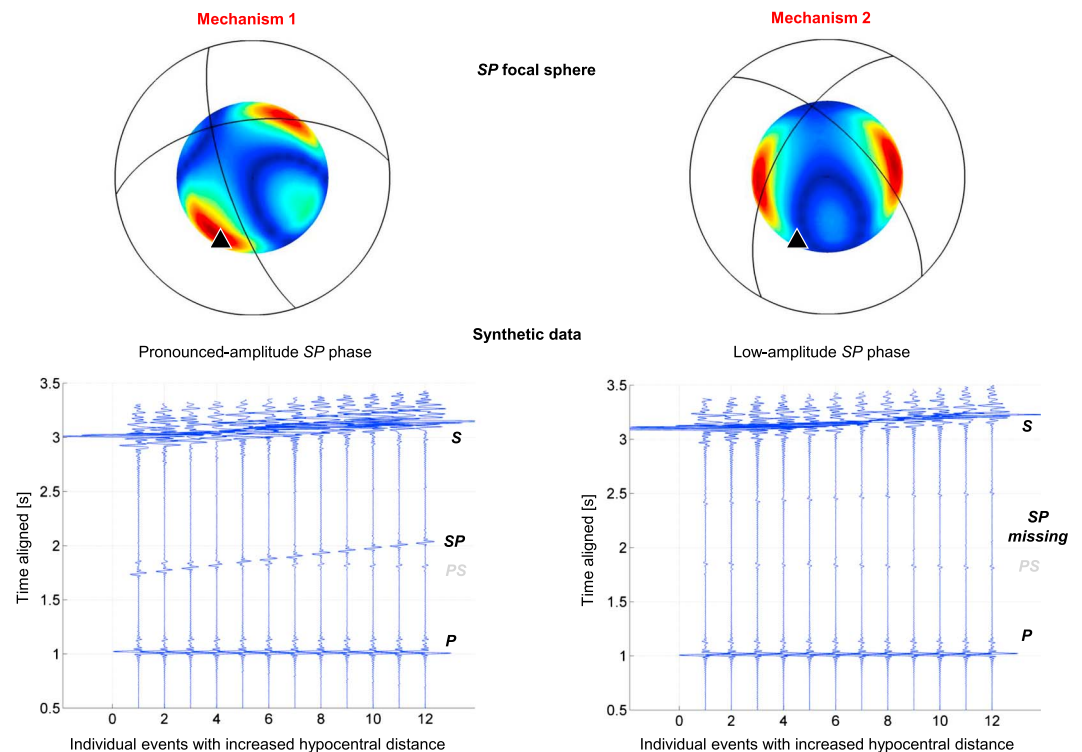


**Figure 6.** (bottom row) Synthetic sections and (top row) the amplitudes of the *SP* conversions on the *SP* focal spheres for two mechanisms characteristic for the analyzed seismicity in West Bohemia. Numerical modeling with the discrete wave number method [Bouchon, 1981] (12 events at variable depths) demonstrates the variation of amplitudes of the *SP* conversions for one station and for the same velocity model but with different mechanisms. The *SP* focal spheres are amplitude normalized from blue (minimum) to red (maximum). Events are plotted with increasing hypocentral distance and *P* wave aligned at 1 s. Note the agreement of the *SP* focal mechanism analysis with the *SP* amplitudes in the synthetics.

In our analysis, we mainly focus on the *SP* converted waves generated at shallow crustal interfaces above seismically active hypocentral zones at depths between 2 and 6 km. At these depths, the *SP* phases are well-pronounced and reasonably separated from the *P* wave coda. In addition, we analyze the *PPP* reflections from local uppermost structure (Figure 2). The *PPP* phases mostly represent reflections from the top of unweathered crystalline rocks or bottom of a sedimentary layer with depths of 200–500 m. Since such phases are prominent in vertical sections, we concentrate on processing of the vertical component recordings. Figure 3 shows two examples of high-frequency waveforms recorded at a single station displaying a prominent *SP* phase. Figure 4 shows the data in the multitrace seismic section view where many events are plotted for one selected station. The waveforms are aligned according to their *P* wave arrival time in order to highlight the *SP* phases.

## 2.2. Data Processing

The extraction of reflected and converted phases generated within the crust is performed in several steps following approach developed by Hrubcová *et al.* [2013] for analysis of the crust/mantle structure. First, we apply the direct *P* wave cross correlation. This enables to detect the exact *P* wave onsets and to align the waveforms according to their *P* wave arrivals (Figure 4). The traces are then ordered with increasing hypocentral distance. The alignment and ordering of traces enhances the coherence of the converted/reflected phases in seismic sections and helps with their identification. Finally, the theoretical traveltimes calculated by ray tracing are associated with the converted/reflected phases. To eliminate the effects of near-surface heterogeneities below stations, the traveltimes of converted/reflected phases are calculated relative to their direct *P* phase arrivals.

## 2.3. Radiation Pattern Analysis

Amplitudes of reflected and converted waves generated by a crustal interface depend primarily on the incidence angle of the wave impinging the interface and on its velocity contrast. However, the amplitudes are also significantly affected by focal mechanism of the earthquake and by source-receiver geometry. Thus,

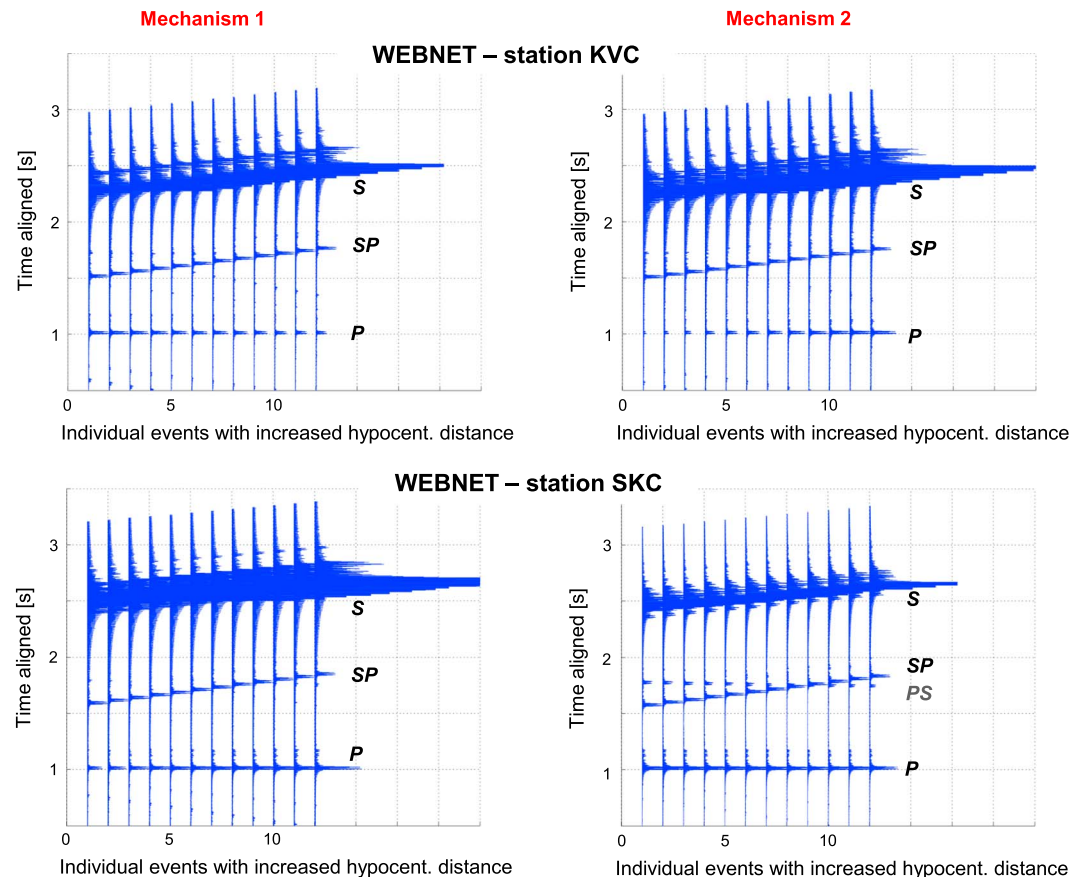


**Figure 7.** Synthetic sections with amplitudes of total vector (in absolute values) calculated for two mechanisms characteristic for the analyzed seismicity in West Bohemia. Numerical modeling with the discrete wave number method [Bouchon, 1981] is illustrated for 12 events at variable depths at WEBNET stations KVC and SKC. Events are plotted with increasing hypocentral distance and *P* wave aligned at 1 s. Note a strong amplitude of the *SP* conversions compared to the *PS* phases which affirms the interpretation of vertical recordings.

missing a significant converted/reflected wave can indicate either absence of an interface in the crust or an unfavorable source-receiver geometry producing low- or zero-amplitude scattered waves. This phenomenon is specific for microseismic data and is missing in processing of other data. For example, the active seismic sources radiate more or less uniformly; and the teleseismic earthquakes produce similar waveforms at stations deployed at a small target area. Thus, analysis of local microseismicity needs special attention compared to standard structure studies. Attention must be paid to focal mechanisms of microearthquakes and their radiation patterns. The stations selected for processing and interpretation must be in directions in which potentially high amplitude converted/reflected phases are expected. A similar approach has been applied by Hrubcová *et al.* [2013] who studied topography of the Moho discontinuity using microseismic data.

Plotting the radiation pattern of the reflections/conversions on focal sphere for a given mechanism is a useful tool in selection of stations suitable for processing in microseismic studies. Figure 5 shows an example of the distribution of the vertical amplitudes of the direct *P* wave (Figure 5a) and of the *SP* conversion (Figure 5b) projected on the focal sphere. The ray directions and amplitudes are calculated using ray theory. The assumed velocity model is isotropic with an interface at a depth of 5 km. The interface has a rather strong velocity contrast of  $0.9 \text{ km s}^{-1}$ . The *P* and *SP* focal spheres are plotted together with two nodal planes defining the focal mechanism. The figure indicates that the amplitudes of the direct as well as converted waves significantly vary over the focal sphere. As expected, the direct *P* wave is zero or negligible close to the nodal lines. The radiation pattern of the *SP* wave is more complicated. First, the zero *SP* amplitude does not follow the nodal lines. Second, the *SP* radiation pattern is defined for a limited interval of ray inclinations. The upper value of the ray inclination from the vertical axis is defined by the ray for which the *S* wave outgoing from

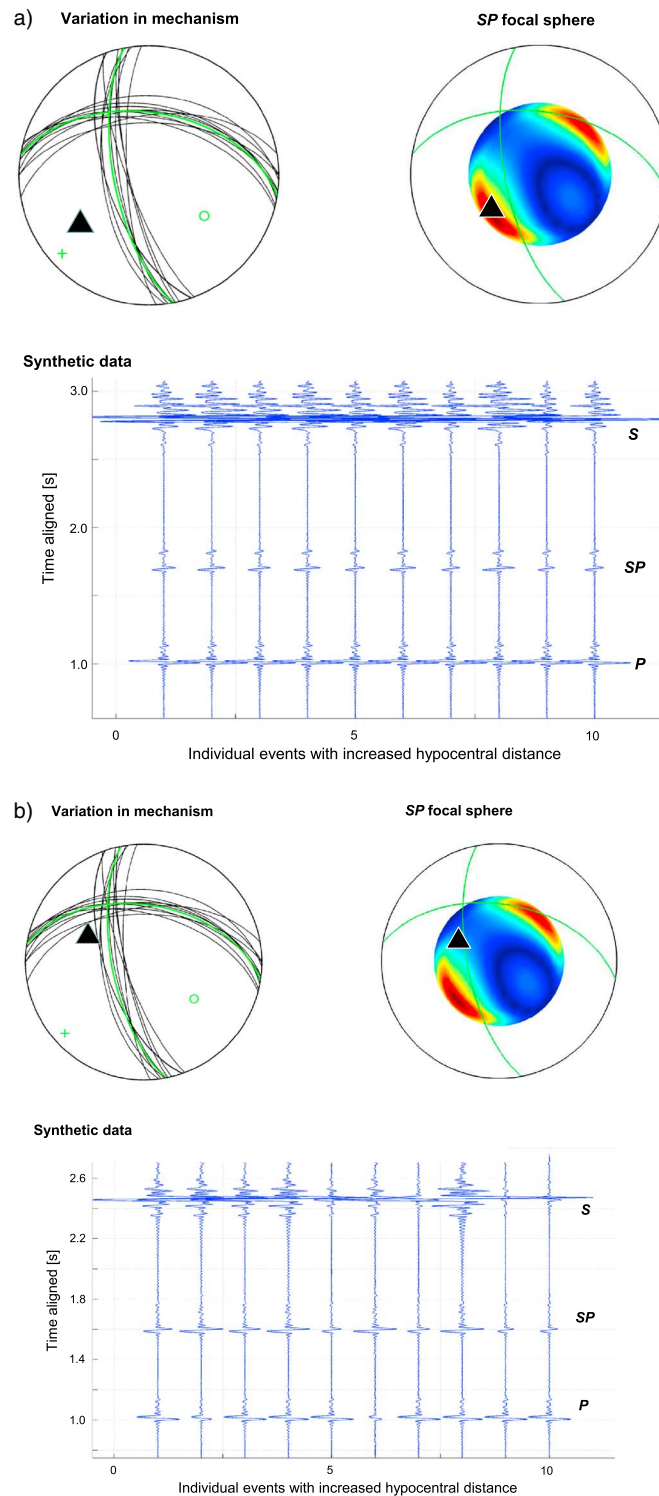


**Figure 8.** Tests of sensitivity of the waveform shape to focal mechanisms. The vertical component waveforms are calculated for strike, dip, and rake varied within  $\pm 10^\circ$  from the mean mechanism. The *SP* focal sphere (amplitude normalized from blue to red) calculated for the average mechanism (green lines). The velocity model and the depth are the same for all events. (a) Stable shape of waveforms for stations far from the nodal lines. Note the same amplitude of the *SP* phases for all events. (b) Unstable (varying) shape of waveforms for stations close to the nodal lines. Note variations in the amplitude ratio between the *P* and *SP* phases with the amplitudes sometimes higher for the *P* and sometimes for the *SP* phases. Green lines, green open circles and plus signs in the focal spheres mark the nodal lines and *P* and *T* axes of the mean focal mechanism. Events are plotted with increasing hypocentral distance and *P* wave aligned at 1 s.

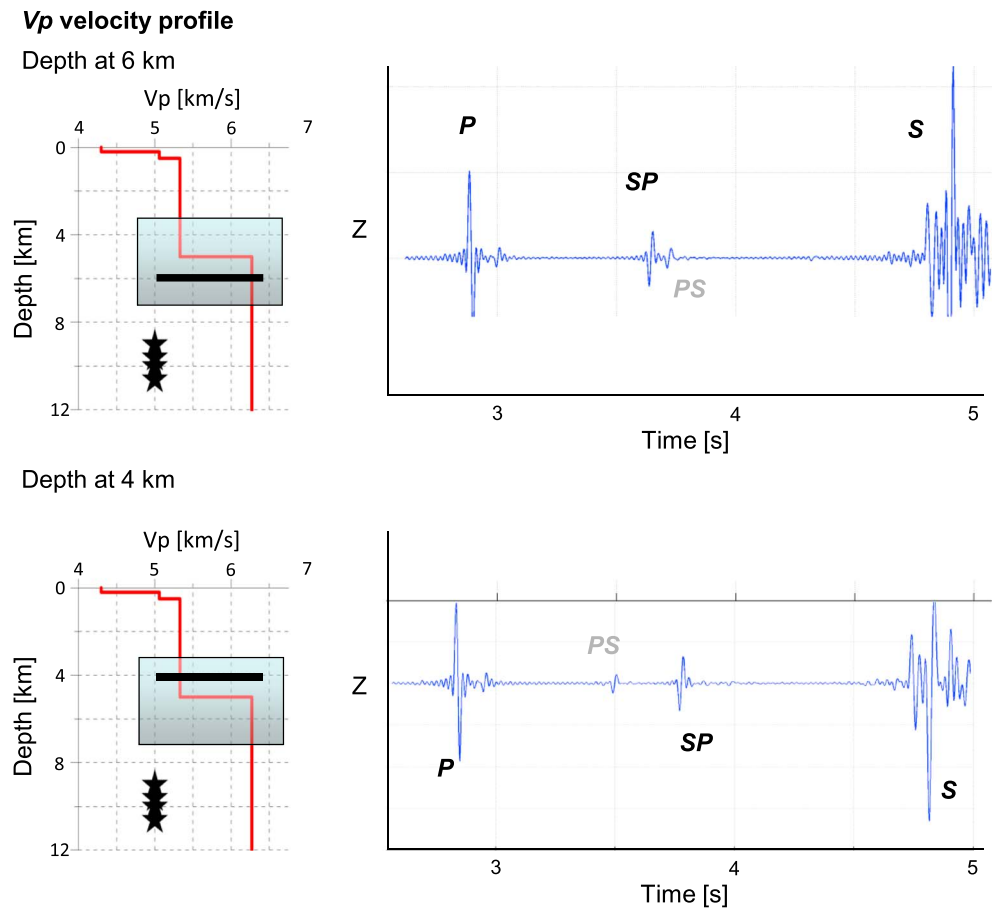


**Figure 9.** Tests of sensitivity of the waveform shape to the velocity model. Vertical component waveforms calculated for two depths of the *SP* conversions (4 km and 6 km). The depth of foci corresponds to the prevailing seismicity in West Bohemia. Note the stable amplitude of the *SP* phase for different discontinuity depths.

the source is converted to the *P* wave propagating along the interface (in a simplified case of two layers this critical angle  $i$  is given according to Snell's law by  $\sin i = V_{s2}/V_{p1}$ ). Suitable stations for processing of the *SP* phase must lie in the red color area in Figure 5b. Obviously, the position of this area on the focal sphere depends on the focal mechanism. So, as demonstrated in Figure 6 (top row), a station suitable for processing for one specific focal mechanism can be quite unsuitable for another focal mechanism.

#### 2.4. Modeling of Synthetic Waveforms

The sensitivity of the converted/reflected waves to focal mechanisms can be well demonstrated on synthetic seismograms. Figure 6 (bottom row) shows the synthetic waveforms for the West Bohemian setting calculated by the discrete wave number approach [Bouchon, 1981]. To simulate observed data, we calculated synthetic waveforms for 12 events located at a depth range of 7.7–10.6 km. The focal mechanisms correspond to two basic types of the mechanisms observed in seismicity in this area [Vavryčuk, 2011b]. We apply real source/receiver geometry as in the WEBNET layout. Synthetic tests are performed for a simple structure with a shallow interface at 0.2 km and a pronounced discontinuity at a depth of 5 km to detect the *SP* and *PS* conversions at individual stations as well as the *PPP* reflections from the uppermost structure.

Figure 6 illustrates the essential influence of focal mechanisms on the waveforms and amplitudes of the *SP* converted waves. Since the station has a different position on the focal spheres of each mechanism with respect to the nodal lines, the amplitudes of direct *P* or *S* waves and the *SP* waves also differ. While the *SP* wave is clearly visible in seismograms of events with the focal mechanism of the first type (Figure 6, bottom left), this wave is missing for events with the focal mechanism of the second type (Figure 6, bottom right). Thus, we have to be



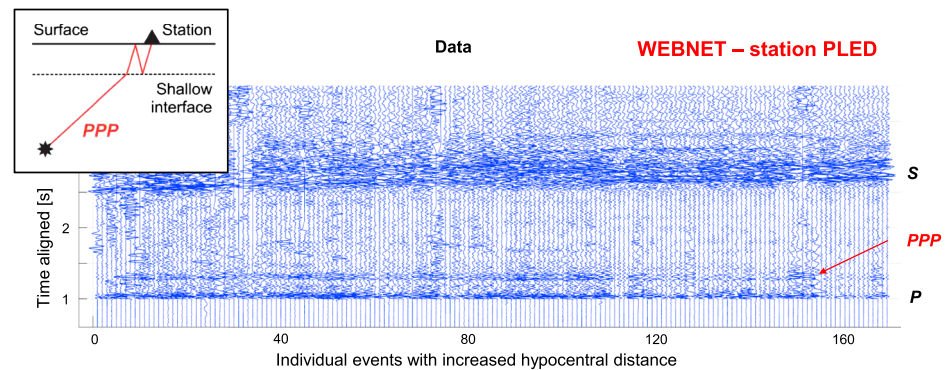
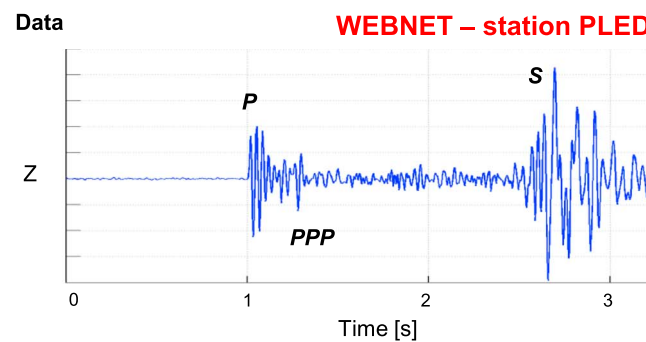


**Figure 10.** Interpretation of the *PPP* phase reflected at a local uppermost discontinuity at station PLED in West Bohemia. Prominent *PPP* phases in vertical recordings arrive 300 ms after the direct *P* waves. Events are plotted with increasing hypocentral distance and *P* wave aligned at 1 s. Note the same time delay of the *PPP* phase for all events.

careful particularly when only indistinctive conversion phases are detected. We have to differentiate two cases: (i) a weak conversion indicating either a missing strong-contrast interface or (ii) indicating just unfavorable radiation pattern of focal mechanism. Thus, it is advantageous to group earthquakes according to their focal

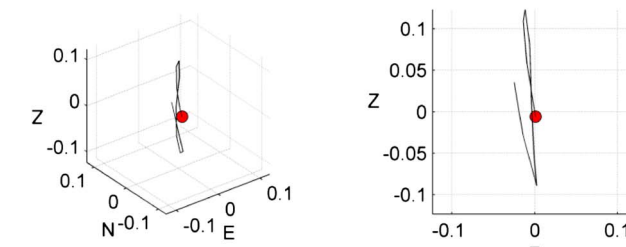
mechanisms and verify by waveform modeling and by calculating the *SP* focal spheres whether the stations are suitable for detecting the crustal interface or not.

Figure 6 documents the *SP* phase as the most pronounced phase at vertical seismic sections. In the case of the *PS* phase analysis, the resolution might be improved by calculating and displaying the total vector which also includes the horizontal components (see Figure 7).



#### Particle motion

*P* wave



*PPP* wave

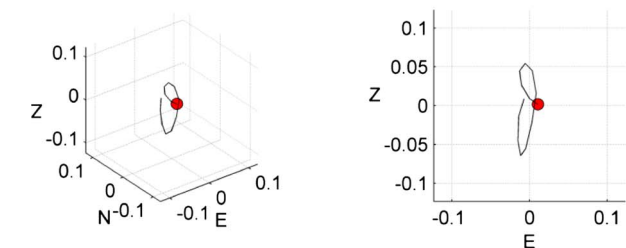


**Figure 11.** Vertical displacement waveform and particle motions for the *P* wave and the *PPP* phase reflected at the uppermost discontinuity (event X2099A at station PLED in West Bohemia). Note similar polarizations of the *P* and *PPP* phase avoiding a misinterpretation of phases.

#### 2.5. Sensitivity Tests

To assess the sensitivity of waveforms to focal mechanisms we run several tests. First, we allow the focal mechanisms of the events of the same type not to be identical but slightly varying. We assume 10 events with similar focal mechanisms calculated by varying the strike, dip, and rake angles of the focal mechanism shown in Figure 6. The variation is random with a uniform distribution in the interval of  $\pm 10^\circ$ . We calculate the waveforms for each event at each station and analyze the variability of the amplitude of the *SP* phase (Figure 8). For most of the stations, the results show stable amplitudes of the *SP* phase and a stable ratio of the amplitudes of the *P* and *SP* phases (Figure 8a). However, for some stations close to the nodal lines,

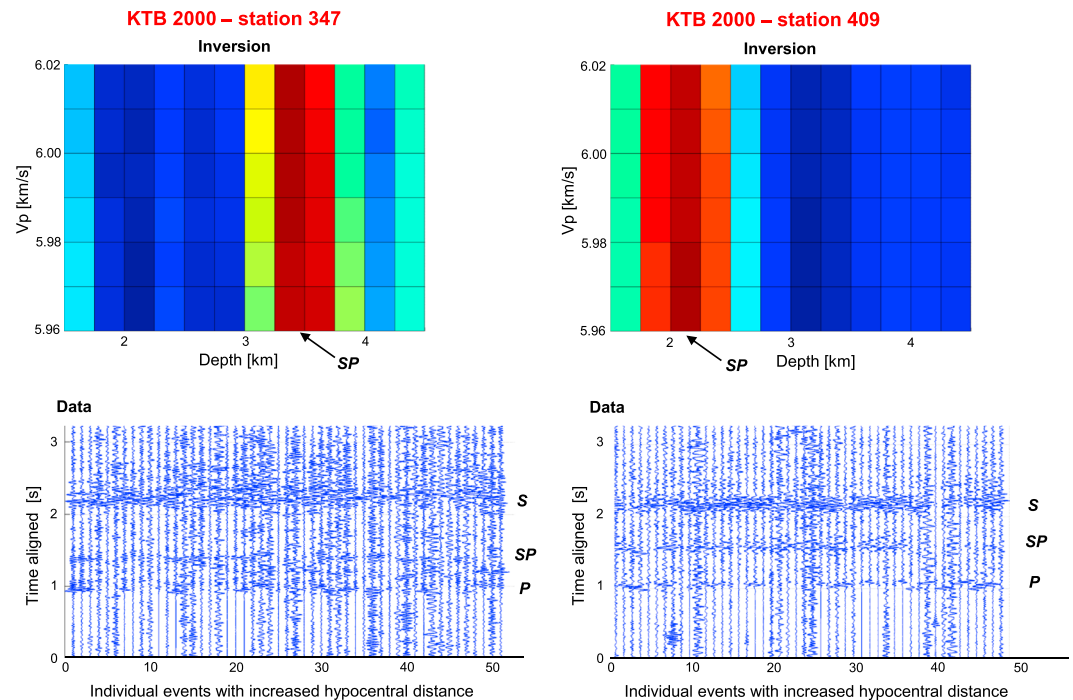


**Figure 12.** Inversion of data from two stations illustrating lateral variations of the discontinuity. (bottom row) Vertical recordings at stations 347 and 409 of the KTB 2000 network with the *SP* conversions. (top row) The inversions indicating a velocity discontinuity at depths of 3.4 km and 1.9 km, respectively. The stacks in the inversion are amplitude normalized from blue (minimum) to red (maximum). Events are plotted with increasing hypocentral distance and *P* wave aligned at 1 s.

the amplitudes of the *P* and *SP* phases vary significantly. We observe waveforms with amplitudes higher for the *P* wave, but also with amplitudes higher for the *SP* phase (Figure 8b). The high sensitivity of amplitudes of the converted/reflected phases on focal mechanism explains the variability of waveforms shown in the multi-trace view (Figure 4). The effect of the waveform variability can be suppressed and partly overcome by processing of large clusters of carefully selected events and by stacking of many traces.

The waveforms of the earthquakes and the amplitudes of the *SP* phase can be also influenced by a depth of the interface. For this reason, we vary the depth of the discontinuity when keeping the same focal mechanism and depth of the event and test the amplitude of the *SP* phase. The calculated waveforms show that the arrival time of the *SP* phase is sensitive to the discontinuity depth, but its amplitude for different depths remains stable. This observation encourages inverting for variations in depth (Figure 9).

## 2.6. PPP Reflections

Except for the frequently observed *SP* and *PS* phases converted at an interface with depth ranging from 2 to 6 km, the high-frequency waveforms sometimes display the *PPP* phase reflected from an uppermost discontinuity beneath the station. This phase behaves differently than the *PS* and *SP* phases. First, it arrives at a given station with the same time delay after the *P* wave for all events irrespective of their depths. Second, since the uppermost shallow structure is strongly laterally variable, the observations of the *PPP* phase are less consistent than those of the *SP* phase when analyzing different stations in the area. Nevertheless, when detected, it can be processed in the same way as the *SP* phase.

An example of the *PPP* phase is presented in Figure 10. This figure illustrates the data for station PLED of the WEBNET network. According to the analysis of the radiation pattern for this station, the *SP* phase is almost invisible in the waveforms. However, the data show a prominent *PPP* phase in vertical sections. Its arrival time is about 300 ms after the *P* wave. A misinterpretation of the *PPP* phase with a converted *PS* phase is avoided by plotting the particle motion (Figure 11). The nearly vertical polarization of this wave indicates a triple *P* wave reflection rather than a converted *P* to *S* wave. This is confirmed by numerical modeling which reveals favorable geometry for this station with a strong *PPP* phase in synthetic waveforms. Taking into account that

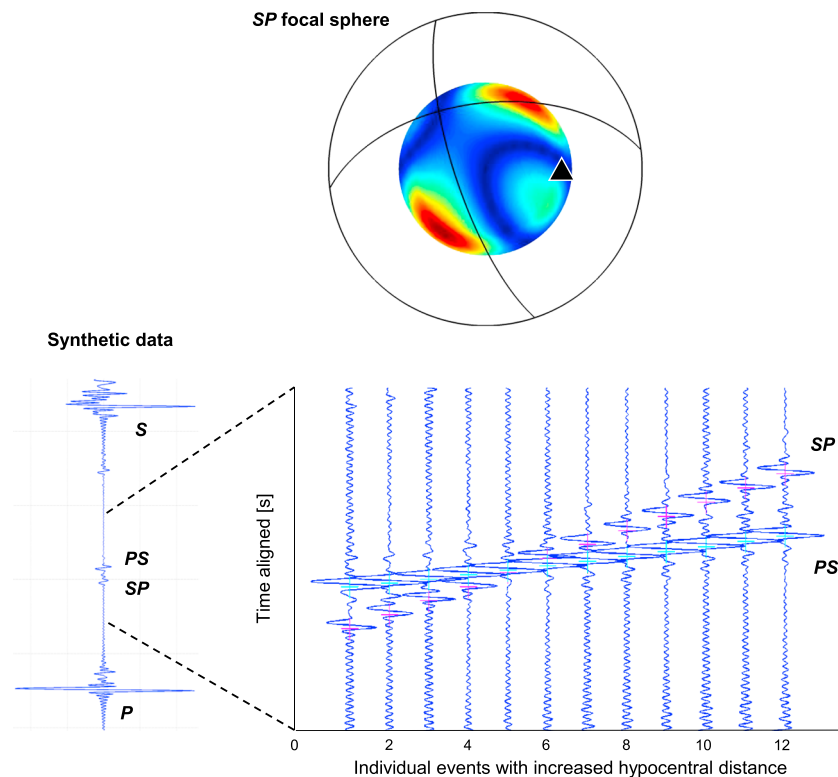


**Figure 13.** Complex pattern of the SP and PS phases documenting the importance of the inversion of stacks of events with foci at different depths. The SP focal sphere for depth of foci in West Bohemia with the position of station HOPD (black triangle). Vertical component synthetic waveforms for events with foci at different depths for station HOPD with the SP and PS phases. Events are plotted with increasing hypocentral distance and P wave aligned at 1 s. Note higher amplitude of the PS phase compared to the SP phase in the vertical records.

the P wave velocity inferred from shallow tomography is in the range of  $3.4\text{--}4\text{ km s}^{-1}$  in the uppermost layer [e. g., Halpaap *et al.*, 2015], the time delay of 300 ms between the P and PPP phases indicates a depth of discontinuity of 500–600 m. Similarly, the SSS phase arriving after the S phase can be detected and interpreted, though its resolution is lower due to the longer and more complex coda of the S wave.

## 2.7. Stacking and Inversion

The inversion for depth of an interface from converted/reflected waves is performed in the following steps. First, the stations suitable for processing are selected using the focal mechanisms analysis. Second, the vertical components of the SP and/or PPP phases at these stations are aligned according to their theoretical arrival times. The arrival times are calculated using two-point ray tracing in a 1-D velocity model. Third, the aligned SP and/or PPP phases are stacked and their total amplitude is calculated. If the velocity model is correct, the aligned waves are in phase, their summation is constructive and the stacked amplitude is high. If not, their summation is destructive and the stacked amplitude is low. Fourth, the velocity model is varied in order to find the highest amplitude of the stack. Specifically, two parameters are searched in a grid: (i) a velocity above the interface and (ii) a depth of the interface. The depths and velocities of the other layers in the velocity model remain fixed. The optimum values of the searched parameters are identified with those which produce the highest amplitude of the stack. The data are processed separately for individual stations in order to evaluate lateral variations of the interface depths (Figure 12).

The importance of stacking waveforms from foci at different depths is documented in Figure 13. This figure shows seismic section for the HOPD station of the WEBNET network where the SP and PS phases are zoomed and magnified. Since the amplitude of the SP phase is low, the PS phase is dominant even in the vertical component. The inversion of a single waveform could result in a misinterpretation of the PS phase and thus in false discontinuity depth. However, when processing a cluster of events with foci at varying depth, the SP and PS phases

are well distinguished by their arrival times and the stacks of the *SP* phase differ from those of the *PS* phase. The phase misinterpretation is removed and the inversion is more reliable. However, if both *PS* and *SP* phases are well visible and separated in time (Figure 13), they can be used for a joint inversion for the discontinuity depth.

## 2.8. Concluding Remarks

Microseismicity is an ideal source of information of local shallow structure. The reflected and converted phases present in the high-frequency waveforms of microearthquakes can serve for identification of discontinuities and determination of their depth within the crust. In our study, we focused on processing of the *SP* and *PPP* phases. These phases are well-pronounced and reasonably separated from the other *P* coda waves so that their interpretation is reliable. Strong dependence of microseismic waveforms on the radiation pattern requires good station coverage of the target area and knowledge of focal mechanisms of the studied microearthquakes. Analysis of real observations must be supported by calculating synthetic waveforms and plotting the radiation patterns of the converted/reflected waves on the focal sphere. The robustness of the inversion for depth of the crustal interfaces is achieved by stacking of a large number of waveforms using a grid search algorithm.

To show basic principles ruling the data and to document data processing and interpretation, we adopt a simple 1-D isotropic velocity model with a few horizontal interfaces. The depth of the interface is retrieved by processing recordings at each station separately. The lateral variations and topography of the studied interface are obtained by interpolating the resultant depths over the whole target area. However, the applicability of this approach is broader not being limited to strictly horizontal structures. For example, the depth of the interface can be retrieved with ray tracing and modeling of synthetic waveforms directly in more complicated structures, e.g., in models with inclined planar or smoothly curved interfaces. In this case, stacking of waveforms is not applied to individual stations but to the whole network.

Another possibility is to perform data processing and interpretation jointly for more phases converted/reflected from the same interface. The processing can be confined to vertical components of the *SP/PS* conversions and *PPP* reflections if phases are well visible and separated in time. It can also be combined with *PS* conversions detected on horizontal components. However, in this case, the horizontal recordings must be rotated according to their radiation patterns and source-receiver geometry (as in Hrubcová *et al.* [2013]). Another option is to perform the analysis of the total vector which also includes horizontal components. Such approaches increase the stability of retrieved results and enhance the robustness of the inversion.

## 3. Application to Induced Microseismicity of the KTB 2000 Fluid Injection Experiment

### 3.1. KTB Drill Site and Tectonic Settings

The Continental Super-Deep Drilling Project (KTB) located in southeast Germany was performed during the period of 1987–1994. Two boreholes were drilled at 200 m distance: the pilot hole reaching a depth of 4 km and the main hole penetrating down to 9.1 km [Emmertmann and Lauterjung, 1997]. Geologically, the KTB is situated at the westernmost part of the Bohemian Massif, just at the contact of the Saxothuringian and the Moldanubian zones (Figure 1). It is close to the Franconian Line, the major thrust-fault zone in the region trending NW-SE. The location of the KTB site was chosen in the Zone of Erbdorf-Vohenstrauß (ZEV), a distinct gneiss-metabasic complex zone that had been tectonically emplaced over the boundary of the Bohemian Massif along the Franconian Line [O'Brien *et al.*, 1997]. Structurally, the ZEV is distinguished from the Saxothuringian and Moldanubian units by its NW striking structures, which are older than the Upper Carboniferous NE trending structures of the other units [Wagner *et al.*, 1997].

### 3.2. Previous Investigations

Reflection profiling was carried out at the KTB site prior to drilling. Apart from the wide-angle reflection DEKORP-4/KTB line [DEKORP Res. Group, 1988], two- and three-dimensional near-vertical reflection studies were performed around the area and the seismic reflection profile KTB 8502 crossing the drill site [Harjes *et al.*, 1997]. These studies gave an insight into the complex structure of strongly deformed inclined metabasites in the vicinity of the drill site determining the continuation of the Franconian Line to depth with the dip of 55° to the NE beneath the drill site. In 1994 and 2000, two fluid injection experiments were performed to study induced seismicity, fluid transport and rock-fluid interactions under crustal stress [Rotherth *et al.*, 2003; Bohnhoff *et al.*, 2004].



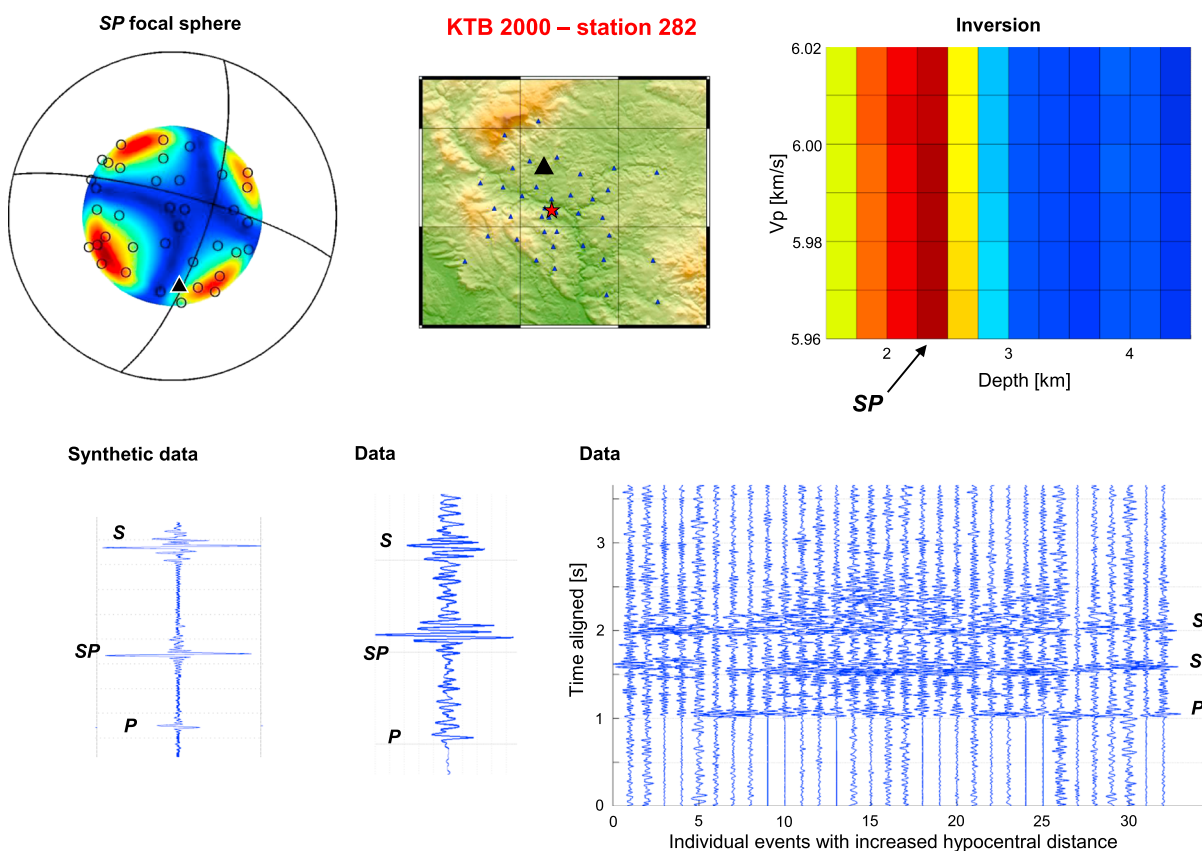


**Figure 14.** Inversion of the *SP* phases recorded at station 282 of the KTB 2000 network. The stacks in the inversion are amplitude normalized from blue (minimum) to red (maximum). The result of the inversion is supplemented by the data (vertical recordings) to demonstrate how the stacked maximum corresponds to the *SP* energy in recordings. The strong *SP* conversions are confirmed by synthetics and by the *SP* focal sphere. The depth of interface is 2.3 km. Events are plotted with increasing hypocentral distance and *P* wave aligned at 1 s. Note the high amplitude of the *SP* phase compared to the *P* phase.

### 3.3. KTB 2000 Fluid Injection Experiment

The KTB 2000 fluid injection experiment lasted for 60 days [Baisch *et al.*, 2002]. The microseismicity was induced by injecting about 4000 m<sup>3</sup> of water. The pressure at the well head ranged from 20 to 30 MPa but the injection phases were interrupted by several sharp pressure decreases during the shut-in stages. The seismicity occurred at depth of the well head (depth of 9.1 km) but also in other depths due to the leaks of fluids in the borehole casing.

The induced seismicity was recorded by 40 three-component surface seismic stations and by one three-component downhole sensor operated in the pilot hole at a depth of 3.8 km. About 2800 induced micro-earthquakes were recorded at the downhole sensor; 237 of them were strong enough to be recorded at and located by the surface stations. The foci were spatially and temporally clustered [Baisch *et al.*, 2002]. The focal mechanisms were computed for 23 events occurring at depth of 9 km and for 125 events at depth of 5 km [Bohnhoff *et al.*, 2004].

### 3.4. Analyzed Data

Microseismic data of the KTB 2000 fluid injection experiment used in this study encompass high-frequency waveforms of 52 events induced at depths of 5.1–5.7 km with local magnitude  $M_L < 1.1$ . We process data recorded by 39 surface three-component stations covering densely the area and with the epicentral distance up to 16 km (Figure 1). The surface stations were equipped with acquisition system PDAS-100 and three-component sensors Mark L4-3C [Vavryčuk *et al.*, 2008]. The sampling rate was 200 Hz. The velocity records are processed by filtering with a band-pass Butterworth filter extracting frequencies between 10 and 40 Hz enhancing signal-to-noise ratio and eliminating low- and high-frequency noise. Extraction of 52 events with the best signal-to-noise ratio results in processing of about 5000 waveforms.

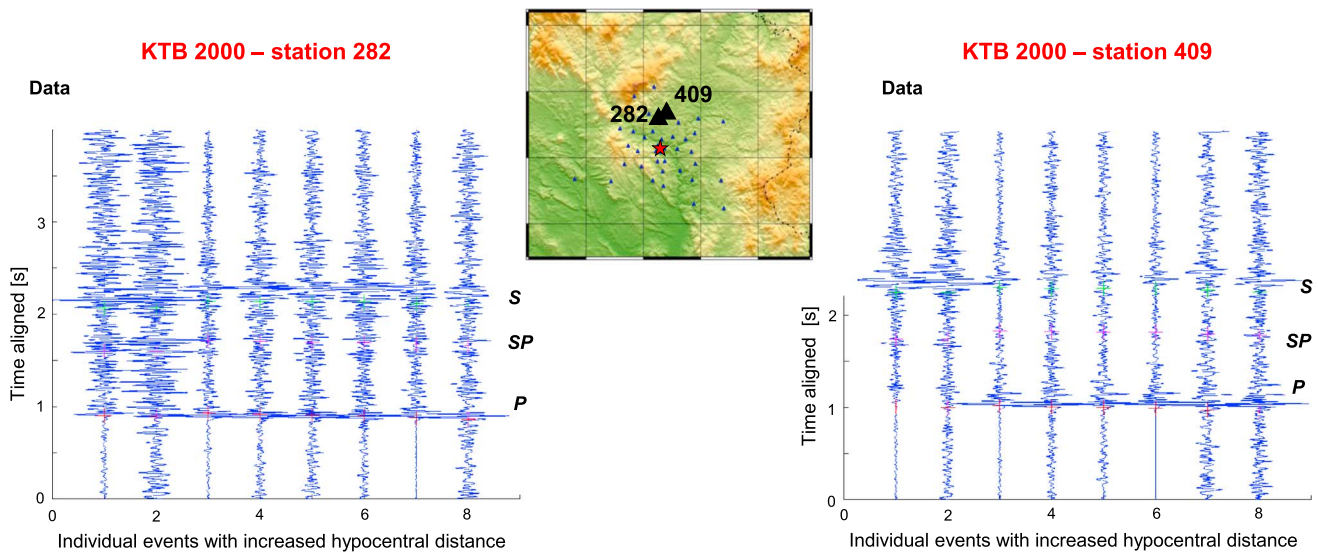
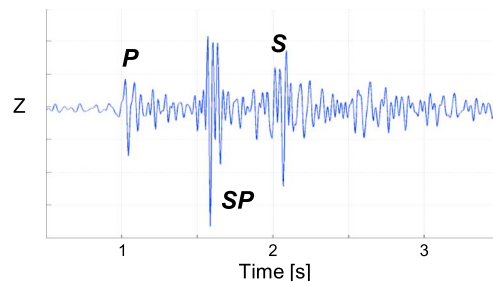


**Figure 15.** Vertical velocity records for stations 282 and 409 of the KTB 2000 network for eight events with foci at depth of 9 km. Events are plotted with increasing hypocentral distance and *P* wave aligned at 1 s. Note the consistent *SP* phases with those from events at depth of 5.4 km (Figures 14 and 12) excluding the possibility of the phase misinterpretation. Color crosses mark the phases.

In our study, we select events with accurately retrieved moment tensors. The fault plane solutions show strike slips with weak normal or reverse components. The *P* and *T* axes are well clustered having their mean azimuth between N320°–340°E and N230°–250°E, respectively. The principal stress axes determined from focal mechanisms were (azimuth/plunge):  $\sigma_1 = 335^\circ/15^\circ$ ,  $\sigma_2 = 110^\circ/70^\circ$ , and  $\sigma_3 = 240^\circ/15^\circ$ ; the shape ratio was estimated to be 0.55. The azimuth and plunge were determined with an error of about 10° [Vavryčuk *et al.*, 2008]. The orientation of the stress axes coincides well with the stress measurements at the KTB site [Brudy *et al.*, 1997] and with the overall tectonic stress in Western Europe.

Data KTB 2000 – station 282



Particle motion

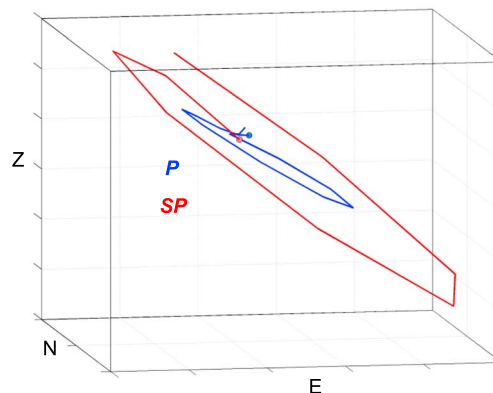


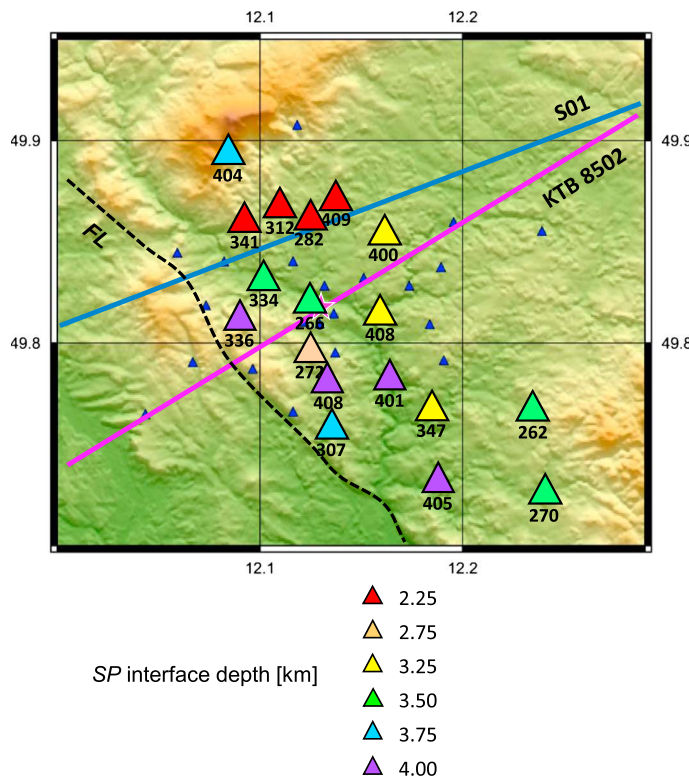
**Figure 16.** Vertical displacement record and particle motion for *P* and *SP* waves (event 023294 from depth of 5.4 km recorded at station 282 of the KTB 2000 network). Note similar polarizations of the *P* and *SP* phases avoiding a misinterpretation with reflection from a steeply inclined interface.

### 3.5. Data Processing

The *P* and *SP* arrival times is calculated by ray tracing in a homogeneous isotropic velocity model, the same that was used for calculation of event locations [Baisch *et al.*, 2002]. The use of such a model is justified because the focal sphere shows good and quite uniform ray coverage, suppressing interferences induced by local inhomogeneities and anisotropy.

The detected *SP* phases are stacked and inverted for the depth of the interface at individual stations. The grid search as a simple and robust method is used for the inversion. We search for two parameters: the interface depth and the  $V_p$  velocity in the layer above this interface. The depth grid step is 0.250 km and the velocity grid step is 0.01 km s<sup>-1</sup>. The effects of near-surface heterogeneities below stations are eliminated by calculation of the converted phases relative to their direct *P* phase arrivals. The stacking is

a) KTB 2000 network



b)

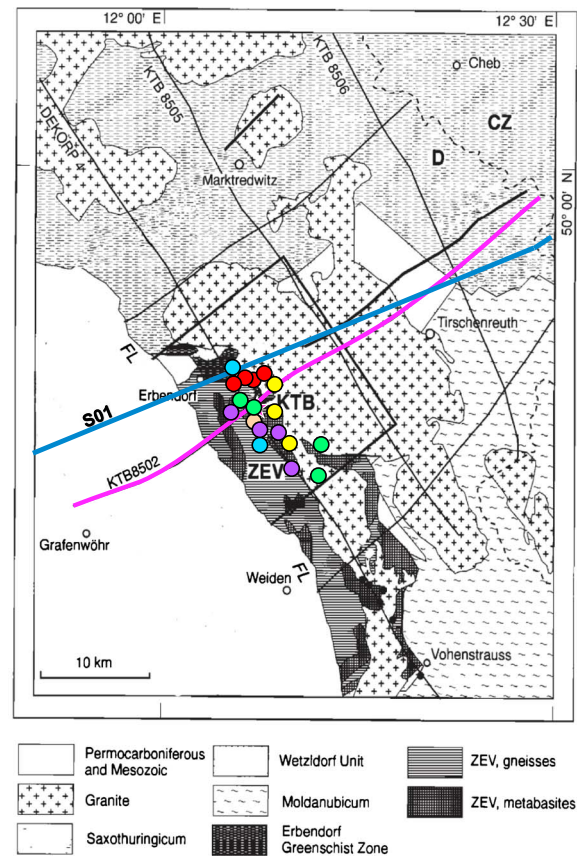


**Figure 17.** (a) KTB 2000 stations with interpreted *SP* conversions at depths of 2.25–4.0 km. (b) Schematic sketch documenting a complicated geological structure near the Franconian Line [after Harjes *et al.*, 1997] with depths of the *SP* interface. The KTB 8502 reflection and S01 refraction lines indicated. The triangles denote stations with the detected *SP* phase; the circles mark the position of the respective interface. FL, Franconian Line; ZEV, Zone Zone of Erbendorf-Vohenstrauß.

done over an interval of 100 ms (representing about 500 m for the velocity of  $5 \text{ km s}^{-1}$ ) so that with the depth grid of 250 m the overlap of the integral stacking vs depth resolution is 1:2. The grid search inversion is done successively for all stations; lateral variations of the interface are traced by the interpolation of the detected interface depths at individual stations.

The inversion of the *SP* phase is demonstrated at station 282 of the KTB 2000 network (Figure 14). The inversion result is displayed along with the data to show how the maximum of the stack corresponds to the well-marked energy of the *SP* phase in the seismograms. Interestingly, the amplitude of the *SP* phase is notably higher compared to the *P* phase. The strong *SP* conversions are confirmed by modeling of synthetic waveforms and by plotting the *SP* focal sphere. The retrieved depth of the interface is 2.3 km. Lateral variations of the interface are visible in Figure 12, where data and inversions are presented for stations 347 and 409 with the interface depth of 3.4 km and 1.9 km, respectively. In such a way, processing of the data from all stations can retrieve topography of the interfaces.

Note that stations at the north (e.g., stations 282 or 409) exhibit very strong *SP* phases (Figure 14). The amplitude of the converted *SP* phase is sometimes even higher than that of the direct *P* and *S* waves. Obviously, this observation looks anomalous and must be checked and tested for phase misinterpretation. For example, we have to rule out whether the phase is not confused with reflections from steeply inclined structures. For this reason, we additionally processed events located at the bottom of the KTB borehole at a depth of 9 km. Based on consistent results obtained from inversions of events located at quite different depth levels, we confirmed our interpretation and excluded the possibility the phase to be reflected from a steeply inclined interface (Figure 15). This result is also confirmed by particle motion analysis (Figure 16). In addition, to keep the time difference between this phase and the *P* phase, critical/overcritical reflections from steeply inclined structures would require a relative velocity contrast of more than  $3 \text{ km s}^{-1}$  which is unrealistic at these depths.



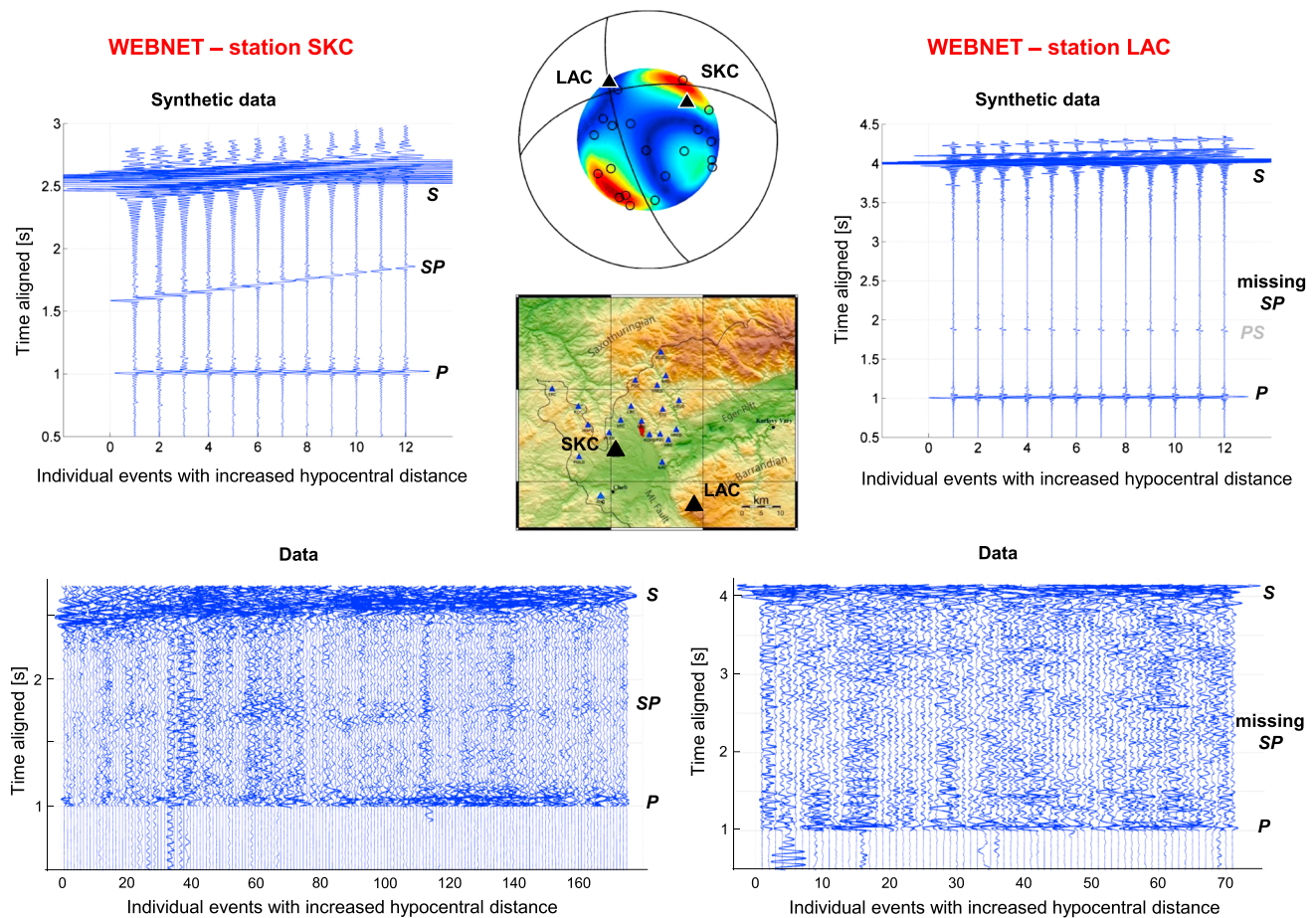


**Figure 18.** Illustration of the sensitivity of waveforms to the radiation pattern and source-receiver geometry. Data are vertical recordings of all analyzed events at the stations SKC and LAC in West Bohemia. The strong *SP* conversions in records of station SKC and the missing *SP* phases in records of station LAC are reproduced in synthetics. Note the agreement of synthetics and data with the position of stations on the *SP* focal sphere. Events are plotted with increasing hypocentral distance and *P* wave aligned at 1 s.

### 3.6. Results

The inversion of the *SP* phase results in the discontinuity at a depth range of 2.3–4.1 km (Figure 17). This interface is the shallowest in the north reaching the depths of 2.1 km and deepens toward the S and SE to 3.5 km and 4.1 km. This finding corresponds with the results along the S01 refraction profile [Grad *et al.*, 2008], which detected a high-velocity body in the upper crust at the contact with the Franconian Line with the velocity contrast of 5.7 to 6.5 km s<sup>-1</sup> at a depth of 2.5–3.5 km.

Such an interface reflects complicated geological structure in the area. The NW-SE trending Franconian Line as the westernmost margin of the Bohemian Massif delimits a distinct gneiss-metabasic complex ZEV (Zone of Erbendorf-Vohenstrauss) tectonically emplaced over the other units [O'Brien *et al.*, 1997]. The ZEV is characterized by dominant NW-SE trending structures and comprises association of metasediments intruded by gabbros, interbedded by lavas and tuffs in an active continental margin or continental rift setting. These structures were also reached by the KTB drill hole showing alternation of inclined gneiss and metabasic sequences [Hirschmann *et al.*, 1997].

Apart from the KTB drilling, inclined structures were also detected by conventional reflection seismic profiling [Hirschmann and Lapp, 1995]. Prominent SE2 reflector located along the KTB 8502 reflection profile at a depth of 3240–4000 m was interpreted as a part of the post-Variscan brittle fault zone of the Franconian Line [Harjes *et al.*, 1997]. For this reason, we also tested a possible misinterpretation of the studied phases for critical/overcritical reflections from steeply inclined structures. However, the analysis excluded this possibility and confirmed the presence of a strong *SP* convertor (see Figures 15 and 16) not related to the Franconian Line.



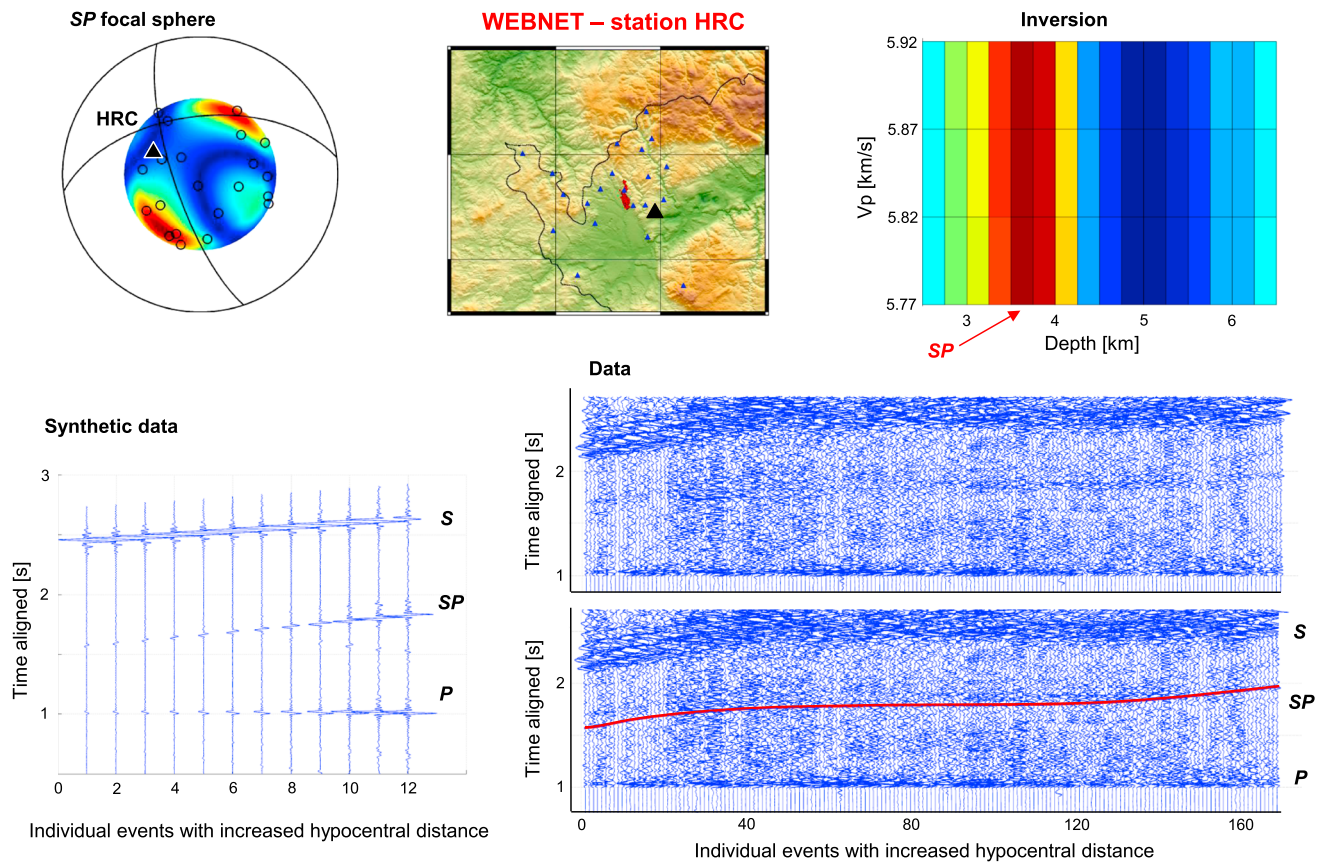


**Figure 19.** The *SP* phase inversion for depth of the interface, station HRC in West Bohemia. The stacks in the inversion are amplitude normalized from blue (minimum) to red (maximum). The *SP* conversions result in a depth of the interface at 3.5 km. Predicted travel times calculated by ray tracing are marked by the red line. Events are plotted with increasing hypocentral distance and *P* wave aligned at 1 s. Note the comparable amplitude of the *SP* phase with the *P* wave, though variable with different depths of events.

In terms of the geological interpretation of the *SP* conversion interface, the Franconian Line bounds the ZEV unit in the west, while in the north and northeast, it is confined by the intrusions of granites of the Hercynian age (see Figure 17b). Thus, the *SP* interface may represent a strong velocity contrast of the granitoids with much faster metabasites underneath. Such interpretation is consistent with the results of 3-D gravity mapping [Emmermann and Lauterjung, 1997], where they attributed the gravity highs near the KTB site to metabasites of the ZEV, and the pronounced gravity lows they interpreted as related to the granites in the NE. The gravity interpretation is in agreement with presence of the *SP* interface especially in places with the granitic rocks outcropping at the surface. In other places, more to the south and west, the *SP* conversions are less pronounced and may represent a contact of individual layers within the ZEV unit with different geophysical properties (e.g., metasediments intruded by gabbros or interbedded by lavas and tuffs).

## 4. Application to Natural Microseismicity in the West Bohemia Swarm Area

### 4.1. Geological and Tectonic Settings

The West Bohemian region is noted for enhanced geodynamic activity expressed by repeated occurrence of intraplate earthquake swarms, fluid degassing, and Tertiary and Quaternary volcanism. The area (Figure 1) is situated at the contact of three Variscan tectonic units: the Saxothuringian, the Teplá-Barrandian, and the Moldanubian [Babuška et al., 2007]. The major faults in the area are represented by the Mariánské Lázně fault with NNW-SSE strike and a fault system with N-S trend [Bankwitz et al., 2003]. The seismicity is relatively shallow with hypocenters located mostly between 5 and 15 km and with local magnitude up to 4 [Fischer et al., 2010, 2014]. The seismic activity is monitored by local seismic stations of the West Bohemian Network (WEBNET) with a uniform and dense station coverage and high-quality recordings.

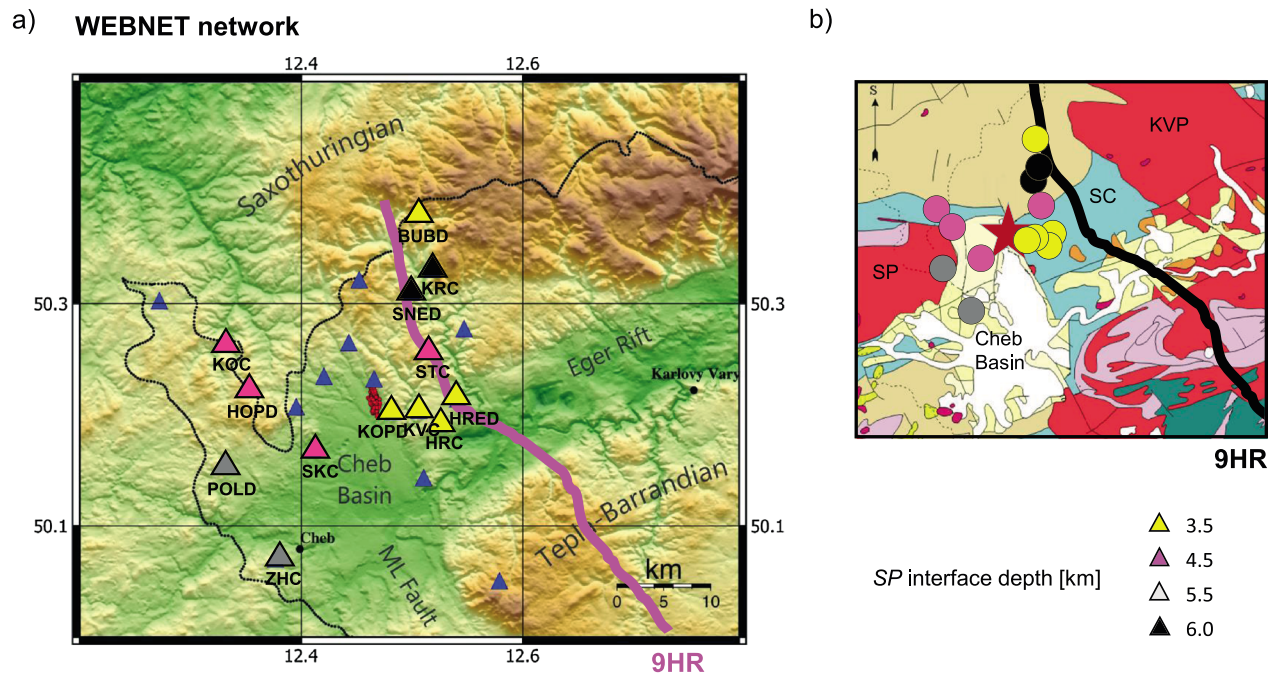


**Figure 20.** (a) Map of the WEBNET stations with the interpreted *SP* conversions at depths of 3.5–6.5 km in West Bohemia. (b) Topography of the conversion interface superimposed on the geological map. The position of the 9HR reflection profile indicated. The red star marks the focal zone. The triangles denote stations with detected *SP* phase; the circles mark the position of the respective interface. KVP, Karlovy Vary pluton; SC, Svatava crystalline; and SP, Smrčiny pluton.

#### 4.2. Previous Investigations

Velocity structure in West Bohemia was a target of several active and passive seismic experiments in the past (Figure 1). Active seismic studies comprised reflection and refraction profiling as MVE-90 [Behr *et al.*, 1994], 9HR [Tomek *et al.*, 1997], CEL09 profile of CELEBRATION 2000 experiment [Hrubcová *et al.*, 2005], or S01 refraction profile of the SUDETES 2003 experiment [Grad *et al.*, 2008]. They targeted the crustal structure including depth of the Moho discontinuity. Passive seismic experiments used temporal and permanent seismic stations and the receiver function method to detect major crustal and upper mantle discontinuities [Wilde-Piórko *et al.*, 2005; Heuer *et al.*, 2006; Geissler *et al.*, 2005]. Discrepancies in the results from active seismic studies and passive teleseismic experiments were investigated by Hrubcová and Geissler [2009].

#### 4.3. The West Bohemia 2008 Earthquake Swarm

The 2008 swarm in West Bohemia lasted about one month. During its course, about 25,000 microearthquakes occurred with magnitude above  $-0.5$  and the largest one reached the magnitude of 3.7 [Fischer *et al.*, 2010; Bouchaala *et al.*, 2013; Vavryčuk *et al.*, 2013]. The events were recorded at 22 three-component WEBNET seismic stations with the epicentral distance up to 25 km (Figure 1). The data set consists of a large number of events located in a small focal zone at depths between 7.6 and 11.7 km. The earthquakes showed basically two types of focal mechanisms and pointed to activating two differently oriented faults [Vavryčuk, 2011b]. The majority of the events were located along almost N-S striking fault (strike  $169^\circ$ ); the fault plane solutions showed oblique left-lateral strike slips. A small portion of events were located along the fault with the strike of  $304^\circ$ ; and the fault plane solutions showed oblique right-lateral strike slips. Both faults are symmetrically oriented with respect to the maximum compression in the region with an azimuth of  $146^\circ$  [Vavryčuk, 2011a].

#### 4.4. Analyzed Data

We processed waveforms of 170 selected events of the West Bohemia swarm 2008. The ray traces and theoretical ray arrival times are computed for the 1-D isotropic velocity model [Málek *et al.*, 2005] used for the event locations. Though some previous studies indicate anisotropic behavior of the West Bohemian Massif [e.g., Vavryčuk, 1993; Růžek *et al.*, 2003; Vavryčuk *et al.*, 2004], the application of the 1-D isotropic

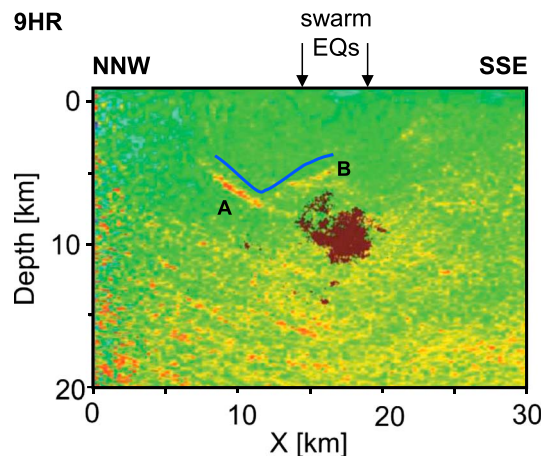


**Figure 21.** The interface from the *SP* conversions in West Bohemia (blue line) superimposed on the reprocessed 9HR reflection profile with two crustal reflectors (A and B) [after Mullick *et al.*, 2015]. The projection of the focal zone of the West Bohemia seismicity is indicated for reference. Note the consistency of both interpretations.

velocity model is justified by the fact that anisotropy is rather weak and highly laterally varying [Vavryčuk and Boušková, 2008], so the overall isotropic velocity model valid for the whole area seems to be a reasonable approximation.

Distinct dependence of amplitudes of shallow converted/reflected phases on focal mechanisms, radiation pattern, and source/receiver geometry is confirmed by synthetic tests. Such tests reveal preferential azimuths suitable for interpretation of data and agree well with observations. As an example, Figure 18 shows seismic sections with vertical velocity recordings of all investigated earthquakes at two WEBNET stations, SKC and LAC. Strong *SP* conversions at station SKC and missing energy from the *SP* phases at station LAC are in agreement with the synthetic seismograms (pronounced-amplitude *SP* phase for station

SKC compared to weak-amplitude *SP* phase for station LAC) and with the position of both stations on the *SP* focal sphere. Similarly, this approach performed well for other stations.

The detected *SP* phases are stacked and inverted for depth of the interface at individual stations. The grid search algorithm works with two parameters: the interface depth (grid step 0.250 km) and the  $V_p$  velocity in the layer above this interface (grid step 0.05 km s<sup>-1</sup>). The effects of near-surface heterogeneities below stations are eliminated by calculation of the converted phases relative to their direct *P* phase arrivals. The stacking is done in an interval of 100 ms (representing about 500 m for the velocity of 5 km s<sup>-1</sup>) so that with the depth grid of 250 m the overlap of the integral stacking versus depth resolution is 1:2. The grid search inversion is done successively for all stations; lateral variations of the interface are traced by the interpolation of the detected interface depths at individual stations.

Figure 19 shows data and results of the inversion for station HRC of the WEBNET network. Strong *SP* conversions are confirmed by the synthetics and correspond to a depth of the interface at 3.5 km. This result also agrees with the *SP* radiation pattern on the focal sphere calculated for this station. The amplitude of the *SP* phase for station HRC is comparable with the *P* wave, though the waveforms vary with depths of events. Similarly as for station HRC, depth of the *SP* conversion interface is retrieved for other stations.

#### 4.5. Results

Analyzing the *SP* conversions at recordings of stations covering the whole area we can map the topography of the *SP* conversion crustal interface. The observations indicate that the depth of the interface varies in a range of 3.5–6.0 km (Figure 20). The lateral variation of the depth displays the deepest part in the NE direction (stations KRC and SNED). The shallowest depths are detected for stations close to the epicenters (stations HRED, HRC, KVC, and KOPD) and also for station BUBD in the north. Such a pattern is not surprising, since the area has a complicated geological structure with the triple junction as the contact of three structural tectonic units (the Saxothuringian, Moldanubian, and Teplá-Barrandian). Local geology is characterized by granitoid pluton (Smrčiny) in the SW and the crystalline metamorphosed phyllites and micaschists of the Saxothuringian (the Svataava unit) in the NE. These rocks underwent complicated geological evolution at the continental margin of tectonic plates during Paleozoic, so that they were folded and thrust over each other. The interface from *SP* conversions probably reflects a contact of granitoids and crystalline rocks underneath. The deepest part may represent the contact of these two units along the fault buried under the Cheb Basin filled with the Tertiary sediments.

A discontinuity with a similar inclination and depth was detected by Mullick *et al.* [2015] who reprocessed the deep seismic reflection profile 9HR intersecting the area [Tomek *et al.*, 1997]. Their high-resolution seismic imaging obtained by applying the Kirchhoff prestack depth migration revealed two prominent inclined reflectors as bright



spots (crustal reflectors A and B in the 9HR refraction profile). Their depth of 4–6 km and place correspond to the interface detected from the *SP* conversions of microseismic sources intersected by the 9HR profile (Figure 21).

Similar discontinuity was detected further to the northwest in Vogtland area, where *Bleibinhaus et al.* [2003] reprocessed a part of the normal incidence reflection profile MVE (distance of 180–310 km) with amplitude preserving 3-D prestack depth migration. They indicated crustal reflectors at depths of 4–6 km. A complicated geological structure reflects also the S01 refraction profile [*Grad et al.*, 2008] slightly more to the south with the second high-velocity body in the upper crust. Its velocity contrast is 5.7–6.5 km s<sup>-1</sup> at depths of 3.5 km which agrees with the detected conversion interface. In a similar way, a double difference tomography from local microearthquake data in West Bohemia shows anomalies in the  $V_p/V_s$  ratio at depths of about 5 km [*Alexandrakis et al.*, 2014] and it may also correspond to the detected interface. Such a discontinuity might be a barrier for seismicity in the focal zone discussed by *Fischer et al.* [2014] and can trap numerous CO<sub>2</sub>-rich emanations of fluids ascending from the mantle and shape the local fluid pathways.

## 5. Conclusions

The structure studies based on microseismic data are specific in several aspects. The waveforms of microearthquakes are of high frequency and complicated. They contain many phases secondarily generated at crustal interfaces and at small-scale inhomogeneities. The waveforms of microearthquakes are highly sensitive to focal mechanisms and thus very different for each station of a local network. At isolated stations, the reflected/converted phase was interpreted by *Sanford et al.* [1973] who identified sharp midcrustal discontinuity from phases after the *S* waves or *Nisii et al.* [2004] who applied moveout and stack of reflected seismic phases to highlight the fit. However, none of such studies considered specific characteristics of local earthquakes with their radiation patterns and thus a systematic analysis was missing. Novel approach in processing and interpretation of scattered waves presented in this study deals with a large number of stations azimuthally distributed around clustered hypocenters of microearthquakes. The waveform analysis of such layout results in the identification of prominent crustal discontinuities and enables the determination of their depths and topography.

Analyzing scattered waves between *P* and *S* waves radiated from microsources, we focused on processing of the *SP* and *PPP* phases well visible on vertical records. These phases are well-pronounced and reasonably separated from other *P* wave coda phases though they need further analyses. We show that strong dependence of microseismic waveforms on the radiation pattern requires good station coverage of the target area and knowledge of focal mechanisms of the microearthquakes. Analysis of real observations must be supported by waveform modeling and by analysis of the radiation patterns of the scattered waves. The robustness of the inversion for depth of the crustal interfaces is achieved by stacking of a large number of waveforms and inverting with a grid search algorithm.

We processed two microseismic datasets of different origin: (i) induced seismicity associated with fluid injections and (ii) natural swarm seismicity. In both cases, the analysis was successful and provided interesting results with tectonic implications. Analyzing the seismicity induced at the KTB site during the fluid injection experiment in 2000, we detected a prominent interface at depths of 2.3–4.1 km, consistent with previous interpretations. Geologically, it may represent the contact of granitoids with much faster metabasites underneath. A detailed mapping of this interface can contribute to understanding the tectonic evolution during the Paleozoic at the westernmost rim of the Bohemian Massif. The high-frequency conversions in waveforms of microearthquakes of the 2008 West Bohemia swarm indicate a strong-contrast interface at depths of 3.5–6.5 km. This interface is probably related to presence of a layer above the focal zone in agreement with the results of previous profiling. The detected interface might be a barrier for shallower seismicity and a trap for emanations of fluids ascending from the mantle.

## References

- Aki, K. (1969), Analysis of the seismic coda of local earthquakes as scattered waves, *J. Geophys. Res.*, 74, 615–631, doi:10.1029/JB074i002p00615.
- Alexandrakis, C., M. Caló, F. Bouchaala, and V. Vavryčuk (2014), Velocity structure and the role of fluids in the West Bohemia Seismic Zone, *Solid Earth*, 5, 863–872, doi:10.5194/se-5-863-2014.
- Ammon, C. J., G. E. Randall, and G. Zandt (1990), On the nonuniqueness of receiver function inversions, *J. Geophys. Res.*, 95, 15,303–15,318, doi:10.1029/JB095iB10p15303.
- Babuška, V., J. Plomerová, and T. Fischer (2007), Intraplate seismicity in the western Bohemian Massif (central Europe): A possible correlation with a paleoplate junction, *J. Geodyn.*, 44, 149–159.

## Acknowledgments

The authors thank J. Horálek and other colleagues of the West Bohemia Network (WEBNET) group for providing the microseismic data from the 2008 swarm activity. This research was supported by the Grant Agency of the Czech Republic, grants 13-08971S, P210/12/1491 and 16-19751J; data acquisition was supported by the project of large research infrastructure CzechGeo, grant LM2010008. Data are available from the authors upon request (pavla@ig.cas.cz). The authors are grateful to the Editor P. Tregoning, Associate Editor, M. Grad, and anonymous reviewer for their valuable comments.



- Baisch, S., M. Bohnhoff, L. Ceranna, Y. Tu, and H.-P. Harjes (2002), Probing the crust to 9-km depth: Fluid-injection experiments and induced seismicity at the KTB Superdeep Drilling Hole, Germany, *Bull. Seismol. Soc. Am.*, *92*, 2369–2380.
- Bankwitz, P., G. Schneider, H. Kämpf, and E. Bankwitz (2003), Structural characteristics of epicentral areas in Central Europe: Study case Cheb Basin (Czech Republic), *J. Geodyn.*, *35*, 5–32, doi:10.1016/S0264-3707(02)00051-0.
- Behr, H.-J., H.-J. Dürbaum, and P. Bankwitz (1994), Crustal structure of the Saxothuringian Zone: Results of the deep seismic profile MVE-90 (East), *Z. Geol. Wiss.*, *22*(6), 647–769.
- Bleibinhaus, F., D. Stich, M. Simon, and H. Gebrande (2003), New results from amplitude preserving prestack depth migration of the Münchberg/Vogtland segment of the MVE deep seismic survey, *J. Geodyn.*, *35*, 33–43, doi:10.1016/S0264-3707(02)00052-2.
- Bohnhoff, M., S. Baisch, and H.-P. Harjes (2004), Fault mechanisms of induced seismicity at the superdeep German Continental Deep Drilling Program (KTB) borehole and their relation to fault structure and stress field, *J. Geophys. Res.*, *109*, B02309, doi:10.1029/2003JB002528.
- Bouchaala, F., V. Vavryčuk, and T. Fischer (2013), Accuracy of the master-event and double-difference locations: Synthetic tests and application to seismicity in West Bohemia, Czech Republic, *J. Seismol.*, *17*, 841–859, doi:10.1007/s10950-013-9357-4.
- Bouchon, M. (1981), A simple method to calculate Green's functions for elastic layered media, *Bull. Seismol. Soc. Am.*, *71*, 959–971.
- Brudy, M., M. D. Zoback, K. Fuchs, F. Rummel, and J. Baumgärtner (1997), Estimation of the complete stress tensor to 8 km depth in the KTB scientific drill holes: Implications for crustal strength, *J. Geophys. Res.*, *102*, 18,453–18,475, doi:10.1029/96JB02942.
- Červený, V. (2001), *Seismic Ray Theory*, Cambridge Univ. Press, Cambridge, U. K.
- Copley, A., and D. McKenzie (2007), Models of crustal flow in the India–Asia collision zone, *Geophys. J. Int.*, *169*, 683–698, doi:10.1111/j.1365-246X.2007.03343.x.
- DEKORP Research Group (1988), Results of the DEKORP 4/KTB Oberpfalz deep seismic reflection investigations, *J. Geophys.*, *62*, 69–101.
- Emmertmann, E., and J. Lauterjung (1997), The German Continental Deep Drilling Program KTB: Overview and major results, *J. Geophys. Res.*, *102*, 18,179–18,201, doi:10.1029/96JB03945.
- Fischer, T., J. Horálek, J. Michálek, and A. Boušková (2010), The 2008–West Bohemia earthquake swarm in the light of the WEBNET network, *J. Seismol.*, *14*, 665–682.
- Fischer, T., J. Horálek, P. Hrubcová, V. Vavryčuk, K. Bräuer, and H. Kämpf (2014), Intra-continental earthquake swarms in West-Bohemia and Vogtland: A review, *Tectonophysics*, *611*, 1–27, doi:10.1016/j.tecto.2013.11.001.
- Fisher, A. T., and K. Becker (2000), Channelized fluid flow in oceanic crust reconciles heat-flow and permeability data, *Nature*, *403*, 71–74, doi:10.1038/47463.
- Geissler, W. H., H. Kämpf, R. Kind, K. Klinge, T. Plenefisch, J. Horálek, J. Zedník, and V. Nehybka (2005), Seismic structure and location of a CO<sub>2</sub> source in the upper mantle of the western Eger (Ohře) Rift, central Europe, *Tectonics*, *24*, TC5001, doi:10.1029/2004TC001672.
- Grad, M., A. Guterch, S. Mazur, G. R. Keller, A. Špičák, P. Hrubcová, and W. H. Geissler (2008), Lithospheric structure of the Bohemian Massif and adjacent Variscan belt in central Europe based on profile S01 from the SUDETES 2003 experiment, *J. Geophys. Res.*, *113*, B10304, doi:10.1029/2007JB005497.
- Halpaap, F., M. Paschke, and F. Bleibinhaus (2015), Structure and tectonics of the Cheb Basin (NW-Bohemia) from a shallow reflection seismic survey, paper presented at EGU 2015 Conference.
- Harjes, H. P., et al. (1997), Origin and nature of crustal reflections: Results from integrated seismic measurements at the KTB superdeep drilling site, *J. Geophys. Res.*, *102*, 18,267–18,288, doi:10.1029/96JB03801.
- Heuer, B., W. H. Geissler, R. Kind, and H. Kämpf (2006), Seismic evidence for asthenospheric updoming beneath the western Bohemian Massif, central Europe, *Geophys. Res. Lett.*, *33*, L05311, doi:10.1029/2005GL025158.
- Hirschmann, G., and M. Lapp (1995), Evaluation of the structural geology of the KTB Hauptbohrung (KTBOberpfalz HB), *KTBOberpfalz HB*, *KTBOberpfalz HB*, *KTBOberpfalz HB*, pp. 285–308.
- Hirschmann, G., J. Duyster, U. Harms, A. Kontny, M. Lapp, H. de Wall, and G. Zulauf (1997), The KTB superdeep borehole: Petrography and structure of a 9-km-deep crustal section, *Geol. Rundsch.*, *86*, Suppl.: 53–514.
- Hrubcová, P., and W. H. Geissler (2009), The crust-mantle transition and the Moho beneath the Vogtland/West Bohemian region in the light of different seismic methods, *Stud. Geophys. Geod.*, *53*, 275–294.
- Hrubcová, P., and P. Šroda (2015), Complex local Moho topography in the Western Carpathians: Indication of the ALCAPA and the European Plate contact, *Tectonophysics*, *638*, 63–81, doi:10.1016/j.tecto.2014.10.013.
- Hrubcová, P., P. Šroda, A. Špičák, A. Guterch, M. Grad, G. R. Keller, E. Brückl, and H. Thybo (2005), Crustal and uppermost mantle structure of the Bohemian Massif based on CELEBRATION 2000 data, *J. Geophys. Res.*, *110*, B11305, doi:10.1029/2004JB003080.
- Hrubcová, P., V. Vavryčuk, A. Boušková, and J. Horálek (2013), Moho depth determination from waveforms of microearthquakes in the West Bohemia/Vogtland swarm area, *J. Geophys. Res. Solid Earth*, *118*, 120–137, doi:10.1029/2012JB009360.
- Koerner, A., E. Kissling, and S. A. Miller (2004), A model of deep crustal fluid flow following the  $M_w = 8.0$  Antofagasta, Chile, earthquake, *J. Geophys. Res.*, *109*, B06307, doi:10.1029/2003JB002816.
- Korenaga, J., W. S. Holbrook, G. M. Kent, P. B. Kelemen, R. S. Detrick, H.-C. Larsens, J. R. Hopper, and T. Dahl-Jensen (2000), Crustal structure of the southeast Greenland margin from joint refraction and reflection seismic tomography, *J. Geophys. Res.*, *105*, 21,591–21,614, doi:10.1029/2000JB900188.
- Langston, C. A. (1979), Structure under Mount Rainier, Washington, inferred from teleseismic body waves, *J. Geophys. Res.*, *84*, 4749–4762, doi:10.1029/JB084iB09p04749.
- Málek, J., J. Horálek, and J. Janský (2005), One-dimensional qP-wave velocity model of the upper crust for the West Bohemia/Vogtland earthquake swarm region, *Stud. Geophys. Geod.*, *49*, 501–524.
- Mayne, W. H. (1962), Common reflection point horizontal data stacking techniques, *Geophysics*, *27*, 927–938.
- Mullick, N., S. Buske, P. Hrubcová, B. Růžek, S. Shapiro, P. Wigger, and T. Fischer (2015), Seismic imaging of the geodynamic activity at the western Eger rift in central Europe, *Tectonophysics*, *647–648*, 105–111, doi:10.1016/j.tecto.2015.02.010.
- Nisii, V., A. Zollo, and G. Iannaccone (2004), Depth of a midcrustal discontinuity beneath Mt. Vesuvius from the stacking of reflected and converted waves on local earthquake records, *Bull. Seismol. Soc. Am.*, *94*(5), 1842–1849.
- O'Brien, P. J., J. Duyster, B. Grauert, W. Schreyer, B. Stöckhert, and K. Weber (1997), Crustal evolution of the KTB drill site: From oldest relics to the late Hercynian granites, *J. Geophys. Res.*, *102*, 18,203–18,220, doi:10.1029/96JB03397.
- Rebaï, S., H. Philip, and A. Taboada (1992), Modern tectonic stress field in the Mediterranean region: Evidence for variation in stress directions at different scales, *Geophys. J. Int.*, *110*(1), 106–140, doi:10.1111/j.1365-246X.1992.tb00717.x.
- Rotherth, E., S. A. Shapiro, S. Buske, and M. Bohnhoff (2003), Mutual relationship between microseismicity and seismic reflectivity: Case study at the German Continental Deep Drilling Site (KTBOberpfalz HB), *J. Geophys. Res. Lett.*, *30*(17), 1893, doi:10.1029/2003GL017848.

- Růžek, B., V. Vavryčuk, P. Hrubcová, J. Zedník, and the CELEBRATION Working Group (2003), Crustal anisotropy in the Bohemian Massif, Czech Republic: Observations based on Central European Lithospheric Experiment Based on Refraction (CELEBRATION) 2000, *J. Geophys. Res.*, *108*(B8), 2392, doi:10.1029/2002JB002242.
- Sanford, A. R., O. Alptekin, and T. R. Topozada (1973), Use of reflection phases on microearthquake seismograms to map unusual discontinuity beneath the Rio Grande rift, *Bull. Seismol. Soc. Am.*, *63*(6), 2021–2034.
- Sato, H., and M. C. Fehler (1998), Seismic wave propagation and scattering in the heterogeneous Earth, AIP Press/Springer, New York.
- Tomek, Č., V. Dvořáková, and S. Vrána (1997), Geological interpretation of the 9HR and 503 M seismic profiles in Western Bohemia, in *Geological Model of Western Bohemia Related to the KTB Borehole in Germany*, edited by S. Vrána and V. Štedrá, *J. Geol. Sci. Prague*, *47*, 43–50.
- Vavryčuk, V. (1993), Crustal anisotropy from local observations of shear-wave splitting in West Bohemia, Czech Republic, *Bull. Seismol. Soc. Am.*, *83*, 1420–1441.
- Vavryčuk, V. (2011a), Detection of high-frequency tensile vibrations of a fault during shear rupturing: Observations from the 2008 West Bohemia swarm, *Geophys. J. Int.*, *186*, 1404–1414, doi:10.1111/j.1365-246X.2011.05122.x.
- Vavryčuk, V. (2011b), Principal earthquakes: Theory and observations from the 2008 West Bohemia swarm, *Earth Planet. Sci. Lett.*, *305*, 290–296, doi:10.1016/j.epsl.2011.03.002.
- Vavryčuk, V., and A. Boušková (2008), S-wave splitting from records of local micro-earthquakes in West Bohemia/Vogtland: An indicator of complex crustal anisotropy, *Stud. Geophys. Geod.*, *52*, 631–650, doi:10.1007/s11200-008-0041-z.
- Vavryčuk, V., P. Hrubcová, M. Brož, J. Málek, and ALP 2002 Working Group (2004), Azimuthal variation of Pg velocity in the Moldanubian, Czech Republic: Observations based on a multi-azimuthal common-shot experiment, *Tectonophysics*, *387*, 189–203, doi:10.1016/j.tecto.2004.06.015.
- Vavryčuk, V., M. Bohnhoff, Z. Jechumtálová, P. Kolář, and J. Šílený (2008), Non-double-couple mechanisms of micro-earthquakes induced during the 2000 injection experiment at the KTB site, Germany: A result of tensile faulting or anisotropy of a rock?, *Tectonophysics*, *456*, 74–93, doi:10.1016/j.tecto.2007.08.019.
- Vavryčuk, V., F. Bouchaala, and T. Fischer (2013), High-resolution fault image from accurate locations and focal mechanisms of the 2008 swarm earthquakes in West Bohemia, Czech Republic, *Tectonophysics*, *590*, 189–195, doi:10.1016/j.tecto.2013.01.025.
- Wagner, G. A., et al. (1997), Post-Variscan thermal and tectonic evolution of the KTB site and its surroundings, *J. Geophys. Res.*, *102*, 18,221–18,232, doi:10.1029/96JB02565.
- Wilde-Piörko, M., J. Saul, and M. Grad (2005), Differences in the crustal and uppermost mantle structure of the Bohemian Massif from teleseismic receiver functions, *Stud. Geophys. Geod.*, *49*, 85–107.
- Yilmaz, O. (2001), Seismic data analysis: Processing, inversion, and interpretation of seismic data, *Soc. of Explor. Geophys.*, doi:10.1190/1.9781560801580.